Title
Study of cellular mechanotransduction by visualizing actin and nucleoskeleton dynamics in real-time

Author
Kan, Shu

Publication Date
2015

Peer reviewed|Thesis/dissertation

Study of cellular mechanotransduction by visualizing actin and nucleoskeleton dynamics in real-time

By

Shu Kan

A dissertation submitted in partial satisfaction of the

requirements for the degree of

Doctor of Philosophy

in

Comparative Biochemistry

in the

Graduate Division

of the

University of California, Berkeley

Committee in charge:

Professor Gerard Marriott, Chair
Professor Fenyong Liu
Professor Constance Chang-Hasnian

Fall 2015

Abstract

Study of cellular mechanotransduction by visualizing actin and nucleoskeleton dynamics

in real-time

by

Shu Kan

Doctor of Philosophy in Comparative Biochemistry

University of California, Berkeley

Professor Gerard Marriott, Chair

Cellular mechanotransduction, the tight coupling between biochemical and mechanical properties of the cytoskeleton and nucleus, drives a large range of cellular processes including cell mobility, cytokinesis, vesicle transportation, or even cell fate determination affected by alterations in gene expression. In this study, we study cellular mechanotransduction by direct imaging of the actin cytoskeleton and component of nucleoskeleton during normal cellular processes and under different stresses.

A novel class of cell permeable actin filament free barbed end dye was developed to achieve high spatial and temporal resolution of actin dynamic imaging. the generation of free barbed ends of actin filaments during lamellipodia protrusion, cytokinesis and endocytosis were monitored in this study, providing new insights on the regulation of free barbed end of actin filaments during these actin-driven processes. By distinguished visualization of the filaments and barbed end pool of actin in cells, the controversial views of whether new actin polymerization is involved during cleavage furrow closure and scission were resolved, we show that there is a surge of new actin polymerization during telophase, beginning with ingression of the contractile ring and ending with the separation of daughter cells, supporting the view that new actin polymerization is involved in cytokinesis.

we further developed a triple labeling system with the genetically encoded florescent protein (FP) fused with nuclear component including emerin, Sun1, Sun2 and lamin A. The FP was carefully choosing so the excitation and emission spectrums of FP and (Si)TMR actin dyes are far apart enough to allow spontaneous imaging of the three components. Several chemicals were applied to disrupt cytoskeleton of the cells, the corresponding responses of the nucleus components were visualized real-time, providing insights on the interaction between nucleus and cytoskeleton.

we also developed a label-free optical biosensor that employs a silicon-based high-contrast grating (HCG) resonator with a spectral linewidth of ~500pm sensitive to ligand-

induced changes in surface properties in collaboration with Professor Constance Chang-Hasnain's group. The device is used to generate thermodynamic and kinetic data on surface-attached antibodies with their respective antigens. The device can detect serum cardiac troponin I, a biomarker of cardiac disease to 100pg/ml within 4-minutes, which is much faster than and as sensitive as current enzyme-linked immuno-assays for cTnI.

To my parents

Table of Contents

Chapter 4.

Acknowledgements

I would like first to thank my advisor, Dr. Gerard Marriott, for giving me the opportunity to do my Ph.D work in his lab. His tremendous passion and enthusiasm for research have been motivating and inspiring me all the times, and his persistent supports and guidance have made everything in my thesis possible. I would also acknowledge all the members of Marriott lab for making the lab an enjoyable place to work.

I would also like to thank Dr. Qing Zhong, who mentor me for the first 3 years of my study in Berkeley, and all the lab members in Zhong lab. I have learned incredible amount from each person.

I also would like to acknowledge my academic advisor Dr. Fenyong Liu, who provide me with advises and persistent supports during my study.

I am grateful to my committee members Drs. Song Li, Connie Chang-Hasnain, and Fenyong Liu for their time and guidance.

Last and most importantly, I have to thank my parents and friends, their believing in my ability to succeed is always a comforting thought.

Chapter 1

Fluorescent Kabarimide C : A novel and selective probe of actin filament free barbed ends and actin polymerization in living cells

Introduction:

The regulation of actin filament dynamics is essential for cell motility, cytokinesis and underlies the intracellular propulsion of pathogens, including Listeria and vaccinia[1-4]. Actin filament dynamics is characterized in living cells by fluctuations in the concentrations and activities of membrane receptors and their effector ligands and proteins including Rac1, Ca2+, PIP2, and CapG and gelsolin, which bind to the protomer at the fast-growing end (barbed-end) and inhibit polymerization. The dissociation of CapG or gelsolin from the barbed end sets in motion a rapid polymerization of actin that is further accelerated by the nucleating protein complexes [5]. Dysfunctional regulation of CapG or gelsolin activity has been linked to poor wound repair, tumor metastasis and inflammation, while intracellular pathogens including Listeria and Vaccinia have evolved mechanisms to trigger barbed-end polymerization of actin at the surface to propel themselves in infected cells. [6]

The protomer at the barbed-end of an actin filament is unique among the thousands of other protomers. For example the barbed end protomer binds selectively to Ca2+-CapG, Ca2+-gelsolin and to nucleating complexes including formin and Arp2/3 [6-10]. Understanding the molecular mechanisms that underlie the regulation of free barbed ends in living cells is made difficult because of the rarity and short lifetime of the free barbed end protomer, and because the field lacks probes that bind selectivity to the barbed-end protomer. In this study we introduce new cell permeable fluorescent probes that function as a small molecule mimetic of CapG and can be used to label dynamically sites of actin filament un-capping in living cells. We have shown in a number of biochemical and structural studies that kabiramide C (KabC; Fig. 1a), a natural product drug isolated from a marine sponge binds to actin protomers in a two-step process [11-13]. The first step involves the interaction of the macrocyclic ring of KabC with residues that line the entrance of the cleft that forms between sub-domains (SD) 1 and 3 at the barbed-end of the actin protomer (Fig. 1b). The second step involves penetration of the hydrophobic tail of KabC into the SD1/3 cleft (Fig. 1c). The combination of these two binding events results in a strong and long-lived KabC-actin complex with sub-nM dissociation constant. The KabC-actin complex is capable of binding to actin filaments through an association of its SD2 with the free SD1/3 cleft on the barbed end protomer, so that the KabC-actin complex now becomes the barbed end protomer. However, since the hydrophobic tail of KabC occupies the SD1/3 cleft in the actin complex it blocks further addition of actin protomers at the barbed end. In this way the kabC-actin complex behaves as a novel constitutively active mimetic of CapG. Since KabC binds to the same site on actin as CapG, gelsolin and profilin, it effectively dissociates these proteins – consequently, on entering the cytosol, KabC molecules will form complexes with actin protomers in the ~100 μM pool of unpolymerized actin. The selective binding of the KabC-actin complex to free barbed end protomers is exploited in this study for the

design of a novel class of probe to image and to quantify the regulation of barbed-ends in living cells. Specifically, we detail experimental conditions that allow fluorescent KabC probes to function as a reporter of free barbed end dynamics in living cells present high spatial and temporal resolution images of KabC probes to provide new insights on the regulation of free barbed end of actin filaments during actin-driven processes including protrusion of lamellipodia, cytokinesis and endocytosis.

Result

Properties of fluorescent KabC probes in cells

TMR-KabC and SiR-KabC are cell permeable and are used to label cytosolic actin in live NBT-II, NIH 3T3, and HeLa cells. The determination of the most effective concentration of each fluorescent KabC for *in vivo* imaging of free barbed ends included considerations of the signal to noise ratio, phototoxicity, impairment of cell division and unusual cell morphologies including blebbing, and generation of dense intracellular vesicles. NBT-II cell incubated at an external concentration of 10nM in the culture medium for at least 60 minutes is the most effective, and allowed dynamic imaging of actin filament free barbed ends in NBT-II cells. The probe proved to be an effective *in vivo* marker of barbed end dynamics for at least 8 hours.

Imaging free barbed ends and actin filaments

The selectivity of fluorescent KabC binding for the actin protomer at the barbed ends of actin filaments in mammalian cells is first demonstrated using high-contrast fluorescence imaging of TMR-KabC and FITC-phalloidin in labeled cells (Fig. 2). Live NIH 3T3 cells are labeled with TMR-KabC by adding the probe from a DMSO stock to culture medium at a final concentration of 10nM for 1 hour, during which time the probe accumulates via passive diffusion in the cytoplasm. TMR-KabC labeled cells are subsequently fixed and labeled with FITC-phalloidin at 1uM for 20 minutes. Fluorescence images of TMR-KabC and FITC-phalloidin show enrichments and an overlap of signals from each probe at the plasma membrane, primarily at sites of lamellipoidial protrusion and membrane ruffling, the cell cortex and on intracellular vesicles (Fig 2). TMR-KabC is absent from stress fibers and focal contacts, whereas these structures are labeled strongly with FITC-phalloidin. The differential staining pattern suggests that TMR-KabC probes molecules are found primarily at sites undergoing active actin polymerization i.e. where free barbed ends are generated. On the other hand, the stress fibers and focal contacts in these cells do not stain with TMR-KabC, which suggests the mature actin filaments in these structures are capped at their barbed ends by capping proteins including CapG and gelsolin and are thereby unable to incorporate new protomers. Drawing form conclusions of our previous studies on the binding and structural properties of KabC [13], we propose that KabC binds selectively to free actin protomers at the barbed ends of the filaments at sites undergoing actin polymerization. These studies are consistent with our preliminary and earlier findings from our group. [12]

Generation of free barbed ends during movement and cell spreading

Having shown that fluorescent KabC probes bind to free protomers at the barbed end of actin filament in fixed cells, we next asked if the probe can provide dynamic information in live cells. Our approach to these studies involved imaging KabC derivatized with a new fluorescent probe based on the silicon-substituted rhodamine molecule (SiR). The KabC probe is prepared by reacting the NHS-ester of SiR (Spirochrome Corp) with an amino substituted kabiramide C probe as described by Petchprayoon et al. [14] The conditions for using SiR-actin as a robe for live cell studies proved to be cell specific, with the staining protocols for NBT-II and HeLa cells being detailed in the Method section.

The Near infra-red (NIR) fluorescence emission from SiR-KabC in NBT-II cells undergoing actin-driven membrane protrusion and motility on a collagen-coated glass surface is imaged using a Zeiss 700 confocal microscope. SiR-KabC fluorescence in resting cells is uniformly distributed within the peri-nuclear region of labeled cells, where it likely forms a 1:1 complex with the cytoplasmic pool of non-polymerized actin protomers [15]. This staining pattern changes dramatically however in motile cells as shown in Fig.3a. In bursts of SiR-KabC staining in the form of micron scale clusters that form a short distance behind the plasma membrane are followed by the formation and protrusion of a lamellipodium. These SiR-KabC clusters dissipate within a few seconds and reappear at new flanking sites that result in a further propagation and extension of the leading edge. Thus waves of bright SiR-KabC clusters that form close to the plasma membrane correlate with membrane protrusion and formation of a lamellipodium. Interestingly, cells that undergo directional motility are characterized by hemispherical lamellipodia that form as a result of breast-stroke line waves of SiR-KabC staining. Based on previous structural and biochemical studies on the complex between actin filaments and KabC we suggest the SiR-KabC labeled clusters are sites where high number of free barbed ends are generated and along with accessory proteins including Arp2/3 and formin, these barbed ends support an explosive polymerization of actin filaments that drives membrane protrusion.

Fluorescence images of SiR-KabC fluorescence in NBT-II cells attached to extracellular matrix protein substrates collagen are shown in Fig. 3b. The SiR-KabC probe is evenly distributed in the cytoplasm of cells during an early stage of attachment. Upon making contact with the ECM substrate, clusters of SiR-KabC fluorescence appear at cell cortex with a diameter of ~ 1 m. These clusters most likely represent early actin filament-associated attachment sites between the cell and the ECM substrate, as in cases where the cell moves slightly after attaching to the substrate the position of the cluster does not change. These clusters grow much larger with a concomitantly brighter fluorescence signal in motile cells and are also seen to propagate in wave-like fashion along the leading edge of the plasma membrane. Again based on a large number of studies in the literature, these dynamic sites of SiR-KabC staining are likely to correlate with the generation of a large number of free barbed ends that undergo explosive waves of polarized actin polymerization that drives cell spreading.

Having shown that fluorescent KabC probes bind to free protomers at the barbed end of actin filament during cell attachment, we next asked if KabC probes can provide dynamic information during other actin-polymerization driven processes within living cells. Our approach to these studies involved dual-imaging of SiR-actin, a jasplakinolide derivative that is known to bond to actin protomers on the side of the filament. SiR-actin, developed by Kai Johnsson's group, is the first cell permeable and red-shifted fluorescent probe that is known to label dynamically the actin filaments in a broad range of cell types [16]. The purpose of imaging SiR-actin and TMR-KabC in the same motile cells is to better understand the regulation of actin filaments during a motile response by resolving at high spatial resolution the generation of free barbed end filaments with TMR-KabC and older or more established actin filaments that are labeled with SiR-Jas (Fig.3c).

The conditions for using both TMR-KabC and SiR-Jas for dynamic imaging are limited and cell specific. In the case of NBT-II cells and other cells detailed in this study the conditions are as follows: NBT-II cells are seeded the night before experiments, and incubated with 100nM of TMR-KabC and/or SiR-Jas for at least one hour before imaging. If both dyes are used in the same cell then the dyes are pre-mixed and loaded together, as it appears the serial uptake of one dye affect the uptake of the second dye. The time delay between the acquisition of TMR and SiR images is less than 1 second, and so overlap images of TMR and SiR include a short temporal offset of no longer than a few seconds – this offset however is very short compared to the timescale of events that lead to changes in the distribution of each probe during a motile response which usually takes minutes or even hours.

NBT-II cells co-stained with 100nM TMR-KabC and 100 nM SiR-Jas for 1 hour do not exhibit any noticeable difference in morphology or motile behavior compared to control cells. Dual imaging of probes for established filaments and those that form dynamically as a result of barbed end uncapping has not been described to date. Our approach allows us to image differences in the distributions of mature actin filaments and free barbed end with high spatial and temporal resolution. Individual frames from a movie of a motile cell are displayed as an image montage in Fig. 3c – sequential images of TMR and SiR emission at 60 second intervals. The arrows with the same color in each frame located at the same position, as showen in 3C**.** in frame 1, The lamellipodium that emerges in the cell is preceded by a burst of TMR-KabC fluorescence at the indicated white arrow. In the following frame (t= 60 secs), the SiR-Jas stain shows the appearance of new actin filaments at the same position indicated by the white arrow. Moreover, a new burst of TMR-KabC staining indicated by the yellow arrow is seen in front of this SiR-Jas signal. The lamellipodium is seen to advance forward and sideways as a consequence of cycles of TMR-KabC fluorescence followed by a forward-moving burst of SiR-Act fluorescence. These dynamic image data suggest that an advancing leading edge arises from the propagation of wave-like signaling clusters that generate free barbed ends that rapidly polymerize in the direction of the plasma membrane. These and related studies strongly support our view that KabC acts as a unique and selective probe for actin protomers at the free barbed end of the filament and that the barbed end capping and uncapping reactions correlate with bursts of actin

polymerization and forward growth of intracellular filaments associated with lamellipodial extensions and motility.

Generation of free barbed ends during PDGF-mediated endocytosis

Endocytosis is a cellular transport process that is often driven by receptor mediated signaling pathways – in its simplest form the binding of a ligand to a cluster of receptors triggers the invagination of the plasma membrane that is pinched off at its neck from the plasma membrane and internalized within the cytosol. The extracellular contents are found in the lumen of the ~100nm diameter endosome. A number of proteins have been implicated in this dynamic process and in the stabilization of the endosome in the cytosol. In particular, actin filaments have long been associated with membrane invagination and the transport of endosomes towards the peri-nuclear region (REFS). For example, previous studies have suggested dynamin and actin work together during clathrin-mediated endosome formation, and it is known that inhibiting actin polymerization by adding the G-actin sequestering drug latrunculin blocks clathrin-coated structures dynamics in neuronal dendrites (REF). Other pharmacological studies have shown endocytic transport is dependent on the actin cytoskeleton, but the mechanism of directional endosome movement during endocytosis is still debating. Fath *et al* had proposed a model of endosome transport where myosin motors attach to endosomes and direct their motility along actin filaments from the plasma membrane to the peri-nuclear region [17]. An alternative mechanism for transport has been proposed by Merrifield et al that indicates endocytic vesicles are transported by propulsive forces that are generated by the polarized polymerization of actin filaments on one side of the endosome to form comet-like tails (rocket-based motility) [18]; This mode of transport resembles that shown by Welch et al for motile Listeria bacteria in infected host cells [19]. Due to the lack of suitable probes to image actin dynamics in living cells, and in particular new sites of actin polymerization, previous studies have employed fluorescence or electron microscopy based imaging of fixed cells and so the dynamic component of these motility mechanisms is lost. In the effort to resolve controversies regarding the mechanism of actin based endosomal transport, and to study the role of barbed polymerization in endocytosis and in the polarized motions of endosomes to the peri-nuclear region, we carried out imaging studies using SiR-KabC and a Fyve domain fusion with GFP as an endosomal maker. The Fyve domain is a conserved protein motif characterized by its ability of bind with high affinity and specificity to phosphatidylinositol 3-phosphate (PI(3)P), a phosphoinositde that is highly enriched on the cytoplasmic side of the early endosome membrane [20]. In our studies, GFP is fused to the C terminus of the FYVE domain from human EEA1 [21]. We show that when this gene is expressed in living cells it produces a FYVE-GFP fusion protein that is restricted to endosomes and allows for endosomal tracking in living cells

Two frames from a movie of TMR-KabC fluorescence in HeLa cells transfected with Fyve-GFP after treatment with 1nM PGDF are shown in figure 4b-c. These cells exhibit robust receptor mediated endocytosis in response to PDGF treatment. Images of a Fyve domain GFP fusion protein expressed in the same cells confirm that the motile vesicles are in fact endosomes (Fig. 4b) rather than other intracellular structures. Our

studies show that only a few endosomes are found in cells before adding PDGF, while the TMR-KabC fluorescence is largely restricted to the plasma membrane.

The rates of endosome formation at the plasma membrane and retrograde motion towards the nucleus increases dramatically after adding PDGF. Overlay images of GFP and SiR fluorescence from the two probes (Fig 4d) show that Fyve-GFP and SiR-KabC colocalizes at sites of actin driven membrane protrusion and occasionally spurns new endosomes resulting in the formation of waves of endosomes that undergo rearward directed motions from the plasma membrane, where they are formed, to the peri-nuclear region. After treatment of PDGF, one can identify two pools of endosomes as indicated by the white and blue arrows in figure 4e. The white labeled endosomes are found close to the cell cortex and are formed prior to the addition of PDGF – these endosomes remain relatively stationary even after PDGF inducing endocytosis and moreover, they do not co-localize with KabC stained clusters. The blue labeled endosomes, on the other hand, form close to the plasma membrane after adding PDGF, as can be seen from the zoomed images in figure 4d, these endosomes move rapidly towards the nucleus. Interestingly, the co-localization of SiR-KabC and the Fyve domain only occurs within the blue-arrow-pool of endosomes. In particular, one can see from figure 4d that the appearance of a new endosome at the plasma membrane is followed by the emergence of a cluster of KabC fluorescence, which trackes the trail-end of endosomes as they move towards nucleus. Significantly the fluorescence of KabC clusters elongates into a tail shape, similar to those that form behind motile Listeria bacteria and vaccinia virus[19, 22], which we argue, is evidence for an actin polymerization driven propulsion of the endosome towards the peri-nucleus region. While actin filaments are known to associate with the endosomal membrane, our findings suggest that their retrograde motion from sites of membrane ruffling involves the generation of free barbed ends and the subsequent polarized actin polymerization at their base.

Generation of free barbed ends during cytokinesis:

Having shown that the fluorescent KabC probes bind to the free actin protomer at the barbed end of the filament at the leading edge of motile cells, we next asked whether free barbed ends are also generated in the cleavage furrow during cytokinesis. A survey of current literature on the molecular mechanism that drives cytokinesis implicates a role for actin filaments de-polymerization in the closure of the contractile ring [23]. On the other hand, Pelham and Chang have presented compelling evidence to suggest that new actin polymerization occurs throughout cytokinesis at least in the case of yeast [24]. If the latter mechanism is correct, then one might expect to see new barbed ends are generated throughout cytokinesis, whereas none are expected if the conventional view is correct. Although the two mechanisms proposed for cleavage furrow closure are completely opposite in terms of the role of actin filaments, they are both consistent with the observed effect. For example, in textbook view of cytokinesis, the driving force for the closure of the cleavage furrow is the contraction of actin bundles in the contractile ring by myosin, which would continue in ever decreasing diameters as filaments are depolymerized. In the alternative mechanism, the ever-decreasing actin ring is continuously formed by new filament growth. We have addressed the controversy of the

role of actin filament dynamics during cytokinesis by imaging the distribution and dynamics of free barbed ends during cell division using the fluorescence of TMR-KabC loaded in NBT-II cells (Fig.5a). NBT-II cells are co-stained with 100nM TMR-KabC and 100nM SiR-Jas with each probe being imaged dynamically as described above. Before cytokinesis, actin filaments exist across the cell cortex as indicated by the SiR-Jas staining, and the the free barbed ends are distributed evenly in the cell cortex with some emphasize on along the plasma membrane. When the cell first enters cytokinesis in frame2, the actin filament start to rearrange to form the cleavage farrow, but at this stage, TMR-KabC is still evenly distributed in the cell; as cell division processes, in frame 3, actin filaments continue to rearrange and further concentrated at the site of cleavage with a much smaller diameter indicating the formation of the contractile ring. The TMR-KabC staining at this point also accumulates and colocalize with the SiR-Jas staining at the site of cleavage, suggesting high concentration of barbed end at the contractile ring, and the continues formation of new actin filaments. At the later frames, the cytokinesis processes further, contractile ring closes with both actin filaments accumulated at the closure and the actin barbed ends.

These imaging studies show that the cleavage furrow is formed via the annealing of existing actin filaments, as revealed by the reorganization and accumulation of SiR-Jas in the cleavage furrow. On the other hand, images of TMR-KabC and SiR-Jas show there is a surge of new actin polymerization during telophase, beginning with ingression of the contractile ring and ending with the separation of daughter cells.

Previous studies have shown that endosomes are delivered to the intercellular bridge during telophase, where they are believed to add membrane to the cleavage furrow [25, 26]. Given our new observations that free barbed end generation and actin polymerization are implicated in the movements of endosome following PDGF treatment, and the role played by endosomes in cytokinesis, we asked if the extensive actin polymerization we observe during the telophase of cytokinesis is responsible for the endosome transport instead of cleavage furrow ingression. Specifically, we tested the hypothesis that the free barbed end generation during telophase does not correlate with the movement of endosomes towards cleavage furrow.

To test the hypothesis, the increase in TMR-KabC staining during ingression and its relation to endosomal transport is investigated by comparing patterns of FYVE-GFP staining during cell division with SiR-KabC.(Fig.5B-C). SiR-Kabc and Fyfe-GFP imaging are carried out in NBT-II cells as detailed above. As can be seen from the time-base image montage shown in Figure 5B, Fyfe-GFP labeled endosomes indeed move towards the cleavage furrow and accumulated along the abscission plane, but when co-stained with SiR-KabC, it is clear the movements of endosomes are not accompanied by the formation of free barbed ends and actin filament propulsion as seen during receptor-mediated endocytosis, suggesting that the directed endosomal transportation to the abscission plate is more likely driven by motor proteins on microtubule or actin filament tracks. On the basis of our studies, we propose that the polymerization of actin filaments during telophase is coupled to the ingression of the actin contractile ring of the cleavage furrow and scission, not the transport of endosomes.

Material and Methods

Preparation of an amino-functionalized KabC probe

KabC was converted into 7-azido KabC via Mitsunobu reaction by using hydrazoic acid as nucleophile in the presence of PPh_3 and DIAD under nitrogen.[14] Then 7-azido KabC was reacted with 3-(fluoren-9-yl-methoxycarbonyl) amino-propyne in the presence of catalytic amount of copper (I) iodide and Et_3N to afford amino protected KabC (KabC-AMT).[14] The structure was confirmed by the presence of aromatic proton signals of Fmoc in the ^1H NMR spectrum. Deprotection of Fmoc with 20% piperidine in dry CH_2Cl_2 gave AMT-KabC. The ^1H NMR spectrum confirmed the triazole proton signal at δ 7.47 ppm and methylene proton signal at δ 4.02 ppm. Compounds were confirmed by ^1H NMR and HRMS (ESI).[14]

Fluorescent KabC probes

KabC derivatives of tetramethylrhodamine (TMR), (Si)TMR (Fig 4A), and the NIR probes IC5-KabC (Fig 4B) and Cy7-NHS were prepared by treating AMT-KabC with the corresponding succinimide ester as described in our earlier publication.[15] For example, a solution of 5-(and-6)-carboxy-(Si)TMR succinimidyl ester (Spirochrome) in DMSO was added to AMT-KabC in dry CH_2Cl_2 100 μL. The reaction was stirred for 8 hours at 20c under nitrogen with the product (Fig. 4B) being isolated by TLC.[15]

Preparation and maintenance of cells

NBT-II cell line was purchased from ATCC, Hela cell line were obtained from Berkeley Tissue Culture Facility. Cells were cultured in high- glucose DMEM with GlutaMAX (Life Technologies, cat. 10566-016) supplemented with 10% FBS (Life Technologies, cat. 16000-085) 1% Penicillin/Streptomycin Solution (Life Technologies, cat. 15140-122) in humidified 5%CO_2 incubator at 37 degree Celsius. Cells were passaged at confluence and seeded in glass-bottom 35-nm dishes (*In Vitro* Scientific, cat. D35-20-1.5-N) 1 night before imaging

FYVE-GFP plasmid was provided by Alexander Hoepker. Plasmid transfection was performed with Lipofectamin 2000(Life Technologies, cat. 11668-019) according to manufacturer recommendations. Cells were seeded at least 8 hours before transfection and grow in a humidified 5% CO_2 incubator at 37 degree Celsius.

Staining of live cell lines

Glass-bottom 35-nm dishes were coated with 50ug/ml Bovine collagen I solutions at 5ug/cm2 for 1 hour at room temperature. Collagen solution was aspirated afterwards and the plates were rinsed with PBS. Cells were seeded in collagen-coated plates one day before transfection or imaging.

KabC probes from a 100uM DMSO stock solution were added to the complete growth medium to obtain the desired final concentration. NBT-II cells were incubated for 1 hour in humidified 5% CO_2 incubator at 37C before imaging. For Hela cells, 2uM of Verapamil was also added to the complete medium with Sir-KabC and incubated at 5%CO_2 37 degree Celsius for 20 minutes. Then HeLa cells were washed with fresh complete medium and incubated for 30 minutes before imaging.

SiR-Jas was provided by Prof. Kai Jonhsson from Ecole Polytechnique Fédérale de Lausanne. Sir-actin was added to the cells from a 1mM DMSO stock solution to the complete growth medium to a final concentration of 100nM, and then cells were incubated in 5% CO_2 incubator at 37 degrees Celsius for 1 hour before imaging.

Chapter 2

Visualizing Mechanotransduction between the cytoskeleton and nucleus in live cells

Introduction

Mechanotransduction is a property exhibited by every cell type and concerns the translation of mechanical stimuli into biochemical responses that affect cell function, proliferation and behavior [27, 28]. The ability for cell to sense and to respond to mechanical perturbations of their microenvironment is essential for development, differentiation and tumor metastasis [29].

Physical stimuli within the extracellular space are likely sensed by proteins at the focal contact and involve distortions of the plasma membrane [30]. A number of critical mechanosensing proteins and cellular components had been identified including stretch-activated ion channels and the force-induced unfolding of extracellular matrix proteins including vinculin? [31, 32]. More recently, several studies have highlight a role for the nucleus or at least the nuclear membrane as a mechano-sensor. Mechano-sensing at the nuclear membrane is thought to by-pass diffusion-based mechano-signalling mechanisms of gene expression, and may involve direct mechano-coupling of a mechanical disturbance in the cell microenvironment via the cytoskeleton to regulatory elements that control gene expression in the nucleus Isermann P, Lammerding J. Indeed, several studies have demonstrated that specific extracellular mechanical stressors can be transmitted through the actin, microtubule and intermediate filament cytoskeleton networks to the nucleus and result in deformations, nuclear membrane may be further relayed via mechanical or biochemical signaling to the inner nucleus where they alter chromatin structure and activate or repress mechano-responsive genes [33-35].

The nuclear envelope (NE) is a highly organized and dynamic double-membranous structure that partitions the nuclear and cytoplasmic compartments of the cell [36]. Its structural and functional integrity is maintained via specific components in the inter and outer nuclear membrane that physically link the cytoskeleton to the nuclear lamina. This linkage was revealed by the association of actin filaments, intermediate filaments and microtubules in the cytoplasmic cytoskskeleton that are specifically anchored at the nuclear envelope by different types of LINC (Linker of Nucleoskeleton and Cytoskeleton) complexes [37-39]. These connections are absolurely essential for normal cell function, and enable the nucleus to maintain its position and tension within the cell during cell migration and differentiation. Moreover these connections mechanically couple the nucleoskeleton to the cytoskeleton and transduce force-induced regulations in gene expression [40-42]. The main component of the LINC complex include outer membrane embedded Nesprins and inner membrane embedded SUNs. Three types of Nesprin proteins, nesprin1, nesprin2 and nesprin 3, exist in mammalian cells with numerous isoforms also being formed by alternative splicing. Nesprin 3, and the giant isoforms of nesprin 1 and nesprin2 bind directly to actin in the cytoskeleton, whereas

their luminal KASH domain binds to the SUN protein, which is embedded within the inner nuclear membrane. In turn, the nucleoplasmic domains of the SUN proteins, interact with other nuclear membrane proteins including emerin, a shorter nesprin isoform as well as the major component of the nuclear cytoskeleton, lamin [37, 39, 43]. Due to its importance in signal transduction, mechanotransduction plays major rules in regulating cell behavior or even differentiation. Multiple studies have showed extracellular stiffness can influence cell shape and migration [44-46]; upregulation of neurogenic and myogenic differentiation markers in human mesenchymal stem cell (hMSC) differentiation was also observed with patterned substrates [47]; biophysical microenvironment can even replace the effect of small-molecule epigenetic modifiers and improve iPSC generation efficiency [48]. More importantly all these cellular processes collectively will influence a broad range of complex biological processes such as development, wound healing and tumour matatesis. In addition to regulate cellular behaviors, impaired mechanotranduction and LINC complex components had been implicated in multiple diseases. More than 80% of LINC mutation associated diseases are cardiac and/or skeleton muscle pathologies including Emery–Dreifuss muscular dystrophy (EDMD) and dilated cardiomyopathy with conduction system defects disease (DCM-CD) which both result from disturbed assemble between nuclear envelope and A-type lamin in nucleo-skeleton [49, 50].

Understanding how biophysical signal transmitted into nucleus will not only provide more insight of the relationship between biophysical extra cellular environment and cell behaviors, but also propose possible therapeutic targets for related diseases.

One important aspect of the mechanism that underlies mechanotranduction is how the nucleus responds to extra-nuclear biophysical stimuli. In this study, we utilize live cell imaging techniques with fluorescent fusion proteins of Sun, nespin and etc, to investigate at a molecular level how the dynamics of cytoskeleton network affect the nuclei membrane and their interactions during specific cellular processes. By visualization of the real time changes of nucleus with different stimuli, we will gain more insight of the relationship between the biophysical extracellular environment and cell behaviors.

Results

Visualization of nuclear and cytoskeleton proteins

In order to visualize the dynamics of the nucleus in living cells, we first need to establish valid protein markers for the nuclear membranes. Members of the LINC complex are expressed in NIH 3T3 cells with genetically encoded florescent fusion proteins GFP or YFP on their C-termini and examined by live cell confocal fluorescence microscopy. As shown in figure 6A-C, emerin-YFP, SUN1-GFP and SUN2-GFP constructs that are transfected in NIH 3T3 cells by lipofectamine and readily expressed within 24h post-transfection. All three fusion proteins are found to localize predominantly at the inner membrane of the nuclear envelope forming a smooth fluorescent ring that corresponds well with the location of the endogenous protein as seen by immunofluorescence.

Moreover, the transfected cells are healthy and undergo proliferation indicating the expression of these genes does not interfere with vital cellular functions. Lamin-GFP was also expressed in NIH 3T3 after lipofectamine transfection, as shown in the fluorescence image of Fig.6D. In this case the fusion protein localizes predominantly to the inner nuclear envelope and in contact with the nucleoplasm. We also expressed nesprin2-mini, a protein fusion that is composed of of the C-terminal actin binding domain and the C-terminal SUN-binding KASH domain. Nesprin 2-mini-GFP fusion protein is also found to localize to the outer nuclear membrane, which is consistent with previous studies. The final nuclear protein marker tested in this work is Histone 2B. Histone 2B is one of the five main histones that organized DNA into nucleosomes within nucleus; specifically, it is required along with H3, H4 and H2A for the assembly of the octameric nucleosome core. The localization pattern of H2B, as seen from fluorescence images of the GFP fusion protein (shown in Fig.6F) reveals it is diffusely distributed in the nucleus that are punctuated by several spots that most likely represent tightly packed heterochromatin regions.

In addition to nuclear proteins, another important component of cellular biomechanical transduction is the cytoskeleton. In our study we focused primarily on the actin and tubulin networks of the cytoskeleton. Fluorescently labeled phalloidin is the most commonly used methods for actin filaments staining, as it generates provides excellent high contrast images of the actin cytoskeleton. However, phalliodin is not cell permeable, and its application to high contrast imaging of actin filaments requires cell-permeabilization. This condition will clearly compromise the dynamic analyses of the cyto- and nucleo-skeletons that are key to our studies [51]. Moreover, since the actin cytoskeleton is a dynamic network playing major roles in cell division, intracellular trafficking and locomotion, one requires specific types of actin fluorophores that generates images within living cells. Previous studies have focused on GFP-actin fusion proteins [52] or other fluorescent-tagged actin-binding proteins including lifeact. [53] These genetically-encoded probes however have had limited success in imaging actin dynamics due to the interference of the fusion proteins with actin polymerization, their inhibition of actomyosin contraction at elevated levels of expression [52] and their nonspecific binding to actin-binding proteins. In our study, we overcome these limitations by using a newly reported cell permeable probe Sir-actin [54] a red-shifted fluorescent conjugate of jasplakinolide that like phalloidin binds to protomers along the side of an actin filament. In addition, we developed a similar cell permeable SiR (or TMR) derivative of kabiramide C, which is unique in its ability to stain the actin protomer at the fast-growing, barbed end of the actin filament as described in Chapter 1. KabC is small molecular mimetic of gelsolin that specifically bind with the barbed end protomer of actins, kabC is covalently linked with the fluoresce probe Sir, as showed in the Fig.7A, it specifically labels the growing end of actin filaments and therefore can provide information of the dynamics of the actin network. In Fig.7B, images of sites of barbed end actin polymerization are made visible using Sir-Kabc, which accumulates in cells after 1-hour incubation and it decorates transiently free barbed ends forming at the leading edge of motile cells.

Together, these cell permeable probes allow us to image in real time and with high-spatial resolution both the dynamics of new actin growth and the distributions of actin filament bundles associated with stress fibers during cellular processes. As shown in Fig.7A, actin filaments in a living cell are labeled within 1-hour of incubating Sir-act at 100nM. The combination of the TMR, SiR probes and GFP-labeled proteins allows for dual and even triple color imaging of proteins in the cyto- and nucleo-cytoskeletons.

Multicolor imaging of live cells

Since the mechano-transduction pathway involves multiple molecular components from both the cytoskeleton and the nucleus, it is important to develop a set of probes that can monitor real time dynamic changes from both sides of the nuclear envelope. In this study, we developed a simple protocol for multicolor imaging in live cells using a combination of both genetically encoded fluorescent fusion proteins and cell-permeable fluorescent probes. Specifically, NBT-II cells were first transfected with plasmid with genetically encoded FPs fused with nuclear envelope proteins, namely emerin and YFP, Sun1 and GFP or Sun2 and GFP. Next we load the same cells with cell permeable probes of the actin and MT cytoskeletons using Sir-act or Sir-tub respectively. Conditions were established for the labeling of NBT-II cells with these cell permeable probes that limited their potential cytotoxicity. The conditions for labeling are cell specific and in principle must be re-established for other cell types. After incubating NBT-II cells for 1h with Sir-act/Sir-tub, fluorescence images are recorded using a Zeiss 700 confocal microscope. The excitation and emission spectrum of YFP and SiR probe are shown in Fig.8D, samples are excited with 488nm laser and 639nm laser for GFP/YFP and SiR probe respectively, minimal (2~5%) power level is used to avoid photo-toxicity effects and photobleaching of the dyes, each probe can be imaged separately to provide real-time imaging based analysis of interactions between the actin network and the nuclear envelope.

A protocol for co-labeling of YFP and SiR-KabC has also been established within NBT-II cells. Since SiR-KabC labels the barbed-end of the actin filament, it provides unique information on sites of new polymerization that are associated with cell protrusion and nuclear remodeling, more intensive signal in certain regions represents active actin polymerization. Nuclear invagination had been found to be a common feature in some cells [55], but its function and mechanism of formation was still undiscovered. In Fig.8D, a NBT-II cell with nuclear invagination was imaged, the nuclear envelope is folded deep into the nucleus creating an over 5um groove. When overlaid with the Sir-KabC image, it is clear that there is a spot with intensive signal at the bottom of the nuclear invagination suggesting actin was actively polymerizing at that spot and is likely the reason of the invagination. Although it is not clear at this point whether continuous protrusion of actin filaments into the nucleus will result in formation of nucleus actin filaments or this protrusion will not precede further to actually penetrate the nucleus, this imaging method can provide more insight on the regulation of the dynamics of nuclear invagination and actin protrusion on the nucleus.

Since KabC probes can provide unique information about the dynamics of actin, we further developed a triple labeling system with the genetically encoded emerin-YFP, Sir-act and TMR-KabC. The excitation and emission spectrums of YFP, Sir and TMR are far apart enough to allow spontaneous imaging of the three dyes in live cell as showed in Fig.8E.

Visualization of the nuclear dynamics with disturbing cytoskeleton

One main aim of our study is to visualizing the dynamic changes of the nucleus with changes of the biophysical environment. Due to the difficulty of creating a changing extracellular environment while imaging, we used a different approach by alter the cytoskeleton to create a dynamically changing extranuclear environment.

Blebbistatin is actin-affecting drug. It inhibits the motor protein myosin-II which alters the contractile forces of the actin network by lower the affinity of myosin with actin [56, 57]. NIH 3T3 cells expressing SUN2-GFP were incubated with 5nM of blebbistatin and the responses of nucleus were imaged by confocal microscope. As showed in figure 9, before addition of the drug, the nuclear membrane is smooth and circular; within 20 minute of incubation, membrane ruffling started to occur, likely resulted from the unbalanced pressure between the nucleus and the actin network of cytoplasm; nuclear volume shrinkage can be clearly observed by half hour of incubation and the ruffling and shrinkage continuous with longer incubation. Interestingly, after incubated for 2 hours, ruffling of membrane gradually disappeared and the nucleus returned to the round shape as showed in Fig.9, but the volume of the nucleus after blebbistatin treatment is notably smaller than before.

This observation suggests the contractile forces from the actin network is important for maintaining the nuclear shape and volume, however, when minor pressure imbalance occurs between the cytoplasm and nucleus, nucleus can adjust to it in a timely manner. We then increased the blebbistatin concentration to 10nM to increase the pressure imbalance and test if the nucleus membrane can adjust to it. As showed in Fig.10, ruffling and volume shrinkage starts within 20 minutes of incubation and continued, at about 1 hour of incubation, the nucleus envelope suddenly exploded into several interconnected pieces and the cell died soon after. This observation suggests that although nuclear membrane is elastic and can sustain certain degree of force imbalance [58], rapid force change across the membrane can result in breakage. It is also interesting that with both concentrations of blebbistatin incubation, the nucleus volume shrinks first suggesting the actin myosin interaction exert outward tensile force on the NE while the nucleoskeleton was holding the membrane inwards to maintain the pre-stressed state, in 5nM samples, the force between the nucleoskeleton and the actin network soon reached balance state with a smaller nucleus, but in 10nM sample, balance did not reach, instead of collapse of nucleus, the volume of nucleus quickly expanded and resulted in an “explosion”. The mechanism of these two contradictory observations is still unknown but it demonstrates the complexity of the regulation of nucleus’ response with biophysical stresses.

To further study the effect of cytoskeleton changes on nucleus, another drug Cytochalisin D (Cyto D) was also introduced to the cells. Cyto D is also an actin-targeting drug, in contrary to blebbistatin, Cyto D disrupt actin microfilaments and inhibit actin polymerization [59-61]. Nuclear membrane ruffling was observed when NIH 3T3 cells were treated with Cyto D for 1h, but unlike the blebbistatin treated cells, even with long treatment of cyto D, the nucleus never returns to its smooth and circular shape. It is also notable that the Cyto D induced nuclear membrane instability is reversible. When the Cyto D is removed, nuclear membrane ruffling stopped and the nucleus resumed its smooth, round shape.

In addition to drugs directly targeting the actin cytoskeleton, we also examined chemicals that can indirectly affect the regulation of actin. Rho-associated protein kinase (ROCK) promotes cellular contraction through two mechanisms, both involve actin stress formation. First, it phosphorylates myosin light chain to increase myosin II ATPase activity and induces actin bundling, which in turn increases stress fiber formation. Secondly, ROCK inhibits the depolymerization of actin filament indirectly by activation of LIM kinase, LIM kinase will further inactivate the actin dissemble protein coflin and therefore preserve existing actin stress fibers in cells [62-64].

We treated emerin-YFP expressing NBT-II cells with the ROCK inhibitor Y-27632 [65], similar with blebbistatin and cytoD treatment, the shape of the nucleus changes from a smooth, circular shape into a less regular shape shortly after incubation. Then there seemed to be a redistribution of emerin-YFP on the NE. Before the treatment, emerin was evenly distributed around nucleus, but after the treatment, significantly more emerin was observed at the inwardly bended region of the NE compare to the rest of the NE, the emerin concentrated region also become more “floppy” and showed with very rapid raffling. Then, with longer treatment of Y-27632, the NE stabilized, emerin became evenly distributed again but the intensity significantly increased, and the nucleus became irregularly shaped with smaller volume.

Cytoskeletons are not only critical for maintaining the integrity of nucleus during interface, but also important for the force generation during cytokinesis. We examined how ROCK inhibitor affects actin arrangement during cytokinesis and overall cell division with the barbed end actin dye Sir-KabC. As showed in Fig.13A-F, before cytokinesis, KabC signal was well spread over the cells with emphasize on the leading edge of lamillopodia. At the onset of cytokinesis, the lamillopodia retracted and cell started to round up, Kabc at this point distributes generally evenly along the membrane, then active actin polymerization started at two equatorial sites of the cell cortex indicated by the intensive kabC staining, the kabC signal ingresses continuously until met in the middle and the midbody structure is formed. Then before the two daughter cells were physically completely cleaved by the abscission process, actin polymerization increase dramatically at the peripheral of the two daughter cell opposing the abscission site visualized by the redistribution of KabC. The daughter cells start spreading before completely detached. On the other hand, in ROCK inhibitor treated cells, the actin behavior at the onset of cytokinesis seemed to be normal with lamillopodial retraction, cleavage furrow formation and equatorial ingression, but when the two ingression point

jointed in the middle, abscission did not occur; actin polymerization is continuously active at the ingression site even after one hour without abscission. In contrast of the rapid actin polymerization around daughter cells in normal cells, the ROCK inhibitor treated daughter cells stay rounded for long time and minimal polymerization were observed in the cell peripheral.

Discussion and future directions

One direct approach to study mechanotransduction between cytoskeleton and nucleus is to visualize their interaction in real time. In our study, we had established conditions for live cell imaging of several genetically encoded nuclear markers including the nuclear matrix markers Lamin A, the inner-nuclear membrane marker Emerin, Sun1 and Sun2 and the outer-nuclear membrane marker Nesprin2. With these markers, the dynamics of nucleus during normal cell cycle and with stresses can be easily visualized.

In addition to nucleus, cytoskeleton plays crucial roles in mechanotransduction as both the force transducer and generator. To visualize actin and microtubule cytoskeleton networks, we utilized a relative new approach with SiR-labeled dyes. SiR is a cell permeable analog of the commonly used florescent dye TMR. SiR-jaspalkinolide (SiR-Jas) was used in our study to visualize the filamentous actin. Jasplakinolide is a small molecule originally isolated from marine sponge, it binds to actin filaments very specifically [66-68]. SiR-Jas composes a few advantages over the traditional method of actin labeling with phalloidin and actin coupled florescent proteins. First, SiR-Jas is readily cell permeable; making them extremely effective in live cell imaging for actin dynamics compare to phalloidin based florescent dyes. Secondly, it is much smaller than any actin coupled florescent protein that would typically be used for fluorescent microscopy which allows for denser labeling of F-actin and more detailed images can be acquired particularly at high resolutions; it is also less likely to interfere with the cytoskeletal dynamics due to its small size. Another new actin labeling probe we used in this study is SiR-kabC and TMR-kabC. Kabiramide C is a molecular mimic of gelsolin and bind selectivity to the barbed-end protomer of actin, in contrast to SiR-Jas which only bind to mature F-actin, SiR-kabc can provide real-time dynamics of actin.

SiR-labeled dye staining had allowed us to perform multicolor live cell imaging because of its simple protocol and great efficiency. When imaging co-labeling of emerin and barbed end actin in NBT-II cells, we observed pushing inward of nuclear membrane by polymerization of actin and the formation of nuclear invagination. The presence of actin in the nucleus has been an intensely studied topic for decades [69-74]; however, how actin is transported into nucleus is still not fully understand. Previous studies had showed that although actin does not carry NLS (nuclear-localization-signal), it can get into nucleus through diffusion due its small size [74]. Formin had been showed to initiate actin polymerization in nucleus to form short and highly dynamic actin filaments [75], but it is not until recently when researchers discovered that the actin filaments running partially or entirely across the nucleus are mainly thin invaginations of cytoplasmic actin into the nucleus [76]. It was suggested they provide an increased opportunity for cytoplasmic-nuclear transfer of specific molecules [55], but the formation of these invaginations are still

unknown and had been observed as a common feature in many type of cells. The observed intensive kabC staining at the bottom of the invagination in our study showed that actin polymerization could be the driven force for the formation of invaginations.

The contractile actin-myosin networks had been shown to generate forces responsible for many cellular behaviors, from cell shape changes and maintenance to tissue remodeling. it is also important for the maintenance of nucleus shape, the nucleus cannot maintain its round shape and proper size with disruption of the actin-myosin network. Another important function of the actin-myosin contractility is formation of the contractile ring during cytokinesis. Previous studies have suggested that the actin filaments undergo intensive de-polymerization during the closure of the contractile ring and the contraction of the actin-myosin network is the main force driving the cleavage furrow ingression and abscission [77]. There had also been compelling evidence in yeast suggesting the new actin polymerization also occurs during cytokinesis at the cleavage furrow and could contribute for the force generation during ingression [24]. In our studies, the cleavage furrow still formed when the actin-myosin contraction was inhibited by ROCK inhibitor Y-27632. And intensive kabC staining was observed at the ingression site, indicating very active new actin polymerization at the leading edges. The ingressions propagate normally until met in the middle, but did not continue to abscission as normal. This behavior suggested that both new actin polymerization and actin-myosin contribute to cytokinesis, actin polymerization might be main driving force for cleavage furrow formation and propagation while actin-myosin contraction is critical for final abscission.

Material and Methods

Emerin-YFP plasmid was a gift from Dr. Yasushi Hiraoka (NICT, Japan), Nesprin-mini, Sun1 and Sun2 plasmid was a kindly provided by professor Karakesisoglou from University of Durham. Cell maintenance, plasmid transfection was performed as described in Chapter 1.

Blebbistatin was purchased form Selleckchem, cytochalasin D was purchased from Santa Cruz Biotech.and Y27632 was purchased from Stemcell Technology.

KabC probes were prepared as described in Chapter 1, and SiR-tub is a kindly gift from Professor Kai Johnsson from Ecole Polytechnique Fédérale de Lausanne. Live cell staining and imaging was preformed as described in Chapter 1.

Chapter 3

High-contrast Grating resonators for label-free detection of disease biomarkers

Introduction

Point of care devices (POC) offer advantages over conventional technologies for biomarker detection including cost and speed while requiring smaller amounts of the sample and reagents. Since diagnostic tests account for an appreciable percentage of the national healthcare budget, the demand for POC devices and decentralized strategies for low-cost analyses of biomarkers in patient samples will likely increase [78-91].

In most cases, the amount of a target biomarker associated with cancer, neurologic and cardiovascular disease in a POC device is determined by recording a change in the intensity of a colored dye or a fluorescent molecule that is generated by way of an enzyme linked immuno-assay (ELISA). [78, 79] ELISA formats while sensitive, suffer from the use of heterogeneous preparations of antibody-enzyme conjugates whose properties may vary widely from manufacturer to manufacturer and batch to batch. In particular the presence of one or more randomly attached enzyme molecule to an antibody reduces the affinity of the conjugate for their biomarker. Moreover, ELISA assays require multiple incubation and wash-steps that increase the complexity of the device and the time to complete an assay. Label-free approaches to detect target molecules offer an attractive alternative to ELISA's. [84-90] High throughput, label-free optical sensing techniques have been described for POC devices including those based on surface plasmon resonance [84, 85,] photonic crystals [86, 87,] integrated micro-cavity, [88, 89] and metal nanohole arrays [90]. While providing sensitive detection, these devices are produced using expensive e-beam lithography, while the need for exact optical alignments and specialized personnel limits their application at remote sites.

We have developed an alternate label-free biosensor that employs a high-contrast grating (HCG) resonator (Figure 15(a), (b)). [92] The high-contrast grating structure generates strong and specific resonances that are sensitive to surface properties under surface-normal excitation with very high efficiency. The resonance quality factor (defined as resonance wavelength divided by the full width half maxima) of these devices was reported here as ~3000 with a refractive index sensitivity ~418nm/RIU, which is higher than related measures reported for other nanostructures [87-90] that also use direct surface-normal coupling. For example the BIND system (which is based on guided-mode resonant filter) [87] and metal nanohole arrays [90].

The binding of a biomolecule to the HCG surface results in a red-shift of the resonance wavelength, a consequence of increasing the effective optical length of the cavity (Figure 15(c)). Tunable laser is used as excitation source and reflected signal is collected by a photodiode at various wavelength (see Method). Spectrometer is

eliminated here to reduce the cost of the measurement. This measurement configuration is enabled by the narrow linewidth and high sensitivity of the HCG device. HCG's are produced en masse and at low cost by using a standard silicon optical lithography and etching (see Method). And can be patterned as 96-well, 384-well or 1536-well formats for high-throughput screening (optically lithography definition). The surface normal input of the probing light beam simplifies the optical alignment of the device. In this study detection antibodies are chemically-linked to the surface of the HCG where they provide a platform for rapid, sensitive and specific detection of disease-associated antigens. [93]

Following myocardial infarction, damaged cardiac muscle cells release troponin I (cTnI) into the blood – the detection of cTnI in serum is a reliable and validated clinical marker of cardiac muscle tissue injury and stroke, affecting ~1 million people in the USA each year [94-98] .ELISA platforms are most frequently used to detect cTnI as they provide for sensitive and quantitative measures of the serum protein. In this study we show how the HCG label-free detection platform can also be used for rapid and quantitive analysis of cTnI in PBS and in serum over a clinically relevant concentration range of 100 pg/ml to 80μg/ml [93].

Results

HCG resonator design, fabrication and characterization.

The HCG is formed from an ultra-thin layer (a few hundred nm) of a silicon grating that is surrounded by material of low refractive index. A schematic of a Si-based HCG resonator with surface-normal optical coupling is shown in Figure 15(a). Unlike other gratings, HCG devices the refractive index contrast is high at both the entrance and exit planes. The large difference in refractive index (contrast) between the grating plane and its surroundings, results in a strong coupling between resonance modes at both exit and entrance boundaries. Resonance happens inside the grating layer, and air/Si and Si/oxide serve as two boundaries of the cavity. By choosing appropriate grating period and grating barwidth, one can produce a HCG design that supports only two resonance modes[92]. Moreover, by choosing an appropriate thickness of the grating layer, the two resonance modes can be made to interfere constructively at the entrance and exit boundaries, resulting in a high-Q resonator with light propagating in the direction normal to the grating plane. We have reported on this phenomenon in earlier publications[92], and so we will only present a brief summary of the principle. First, if we define ρ as the coupling coefficient matrix between the resonance modes at the entrance/exit boundaries, and φ as the propagation factor inside the Si grating layer, and C is the vector representing a self-sustainable mode that satisfies the round-trip condition. We can show that:

$$C = \rho\varphi\rho\varphi C. \quad (1)$$

The intrinsic quality factor is calculated by

$$Q = \frac{2\pi n_g t_g}{\lambda}\left|\frac{r}{1-r^2}\right|. \quad (2)$$

where t_g is the thickness of the grating, λ is the wavelength of the incident light, n_g is the group index, and r represents the eigenvalues of matrix $\rho\varphi$.

A detailed analysis of the design algorithm employed for the HGG resonator is described in Sections 1 & 4 of reference 16. For the HCG devices used in this study, the period is 792nm, the bandwidth is 427nm, and the grating thickness is 500nm. A test array with thousands of single HCG resonators can be patterned during a single exposure, enabling low-cost and high-throughput production of devices. An SEM image of gratings within a single device is shown in Figure 115(b) and serves to highlight the high quality of structures that are generated using our fabrication process.

A single mode fiber is used to excite resonances inside the HCG sensor– in practice the fiber is simply adjusted vertically above the surface of the HCG to excite resonance, and we find the device works well without the need for a precise optical alignment (Figure 15(d)). The reflection spectrum (see Methods) obtained under fiber illumination of a HCG device is shown in Figure 15(e). It shows that the device has a quality factor measured at ~3000 with a center wavelength of 1564nm when immersed in phosphate buffered saline (PBS).

An important advantage of the HCG resonator over other on-chip resonance based devices is its intrinsic ability to establish a unique pattern of resonance modes. A simulated mode pattern at resonance for an HCG resonator excited with a Gaussian beam of ~10μm spot size (output from a single mode fiber) is shown in Figure 16(a). The top view of the resonance (at 1564nm) sliced through the center of resonator is shown in Figure 16(a). Efficient optical coupling of the input light to the HCG device is facilitated by the large mode overlap between the input Gaussian beam and the resonance mode. The side view of the resonance inside one grating period of the HCG is shown in Figure 16(b), which reveals a large portion of the resonance mode exists near the HCG surface. This feature results in a strong interaction between the resonant light and surface attached biomolecules.

Sensitivity of the HCG device to changes in refractive index.

Quantitative measurements are used to evaluate the intrinsic sensitivity of the HCG device to a change in refractive index. First the sensor is covered uniformly with a liquid of known refractive index (RI), with solvents covering a RI range from 1.494 to 1.506. The results of these measurements are shown in Figure 17(a), and reveal that an increase in RI shifts the resonance wavelength to the red. The shift in wavelength as a function of the change in RI is plotted in Figure 17(b). This plot reveals a linear relationship exists between RI and the red-shift, and shows our HCG sensors have a RI sensitivity (RIS) of 418nm/RIU, which is higher than those measured for other dielectric structures. [86, 87] The high sensitivity of the HCG is attributed to the special resonance mode pattern of the HCG resonator, which was described in the previous section.

Quantitative analysis of antibody-antigen interactions using HCG sensors.

To characterize the sensitivity of the HCG sensor in detecting target antigens, we tested a complementary antibody-antigen pair of unlabeled IgG from rabbit serum (Sigma, I5006) as the antigen, and anti-rabbit IgG produced in goat (Sigma; R2004) as the detection antibody. A schematic of antibody-antigen binding assay platform is shown in Figure 18 (a) and (b). First the HCG sensor surface is linked to the anti-rabbit IgG antibody using a maleimide-thiol coupling reaction (see Methods). Before adding the target antigen, the spectral response of the sensor is recorded and the resonance wavelength for the measurement assigned as the reference. Next solutions (200μl) of the rabbit IgG (antigen) are added separately to the HCG surface over a concentration range from 0.1ng/ml to 1mg/ml. The spectrum is recorded after the addition of each concentration of antigen.

Spectral data of the interaction between surface-bound goat anti-rabbit IgG and rabbit IgG studies are presented in Figure 18(c) and (d). A standard curve for the device is generated by recording the spectral shift for different concentrations of the purified antigen in PBS; three parallel titrations are performed for each antigen concentration to improve the precision of the measurement. The standard curve recorded over a 1000-fold range of antigen concentration shows the shift of wavelength is proportional to the concentration of antigen. The signal associated with the binding of antigens to the surface antibody saturates at ~3 g/ml. The lowest detectable concentration of antigen is 100pg/ml, which results in a wavelength shift of 60pm (red trace of Figure 18(d)). A negative control experiment is carried out using a non-complementary antigen, namely anti-rabbit IgG and mouse IgG, which is shown in the blue line of Figure 18 (d). This wavelength shift for the control sample is minimal compared to the complementary rabbit IgG/anti-rabbit IgG system. The same antibody-antigen complex is detected equally well for rabbit IgG dissolved in serum rather than PBS, which suggests that non-specific binding of serum proteins to the HCG surface is low. Three known concentrations of rabbit IgG in serum (2ng/ml, 10ng/ml and 80ng/ml) lie close to their expected values on the standard curve (black triangles in Figure 18 (d)).

To demonstrate the ability of the HCG device to record dynamic interactions between an antigen and surface-linked antibodies we recorded the shift in the resonance wavelength after adding rabbit IgG binding to the anti-rabbit IgG labeled surface. The spectral response to antigen binding is recorded continuously after the addition of 4 different concentrations of the antigen. As shown in Figure 18 (c), the spectral shift increases exponentially with a time constant of ~50 seconds (on average) and reaches a plateau at 95% of the equilibrium value within 200 seconds. This study shows the HCG devices van be used to quantify the amount of antigen in a sample and to establish kinetic constants associated with complex formation (or dissociation) within 4 minutes.

Quantitative analysis of cardiac Troponin I.

Purified human cTnI is detected in serum and PBS using a commercial anti-human troponin I antibody that binds to an epitope between residues 86-209 on troponin I (sc-

133117, Santa Cruz Biotechnology). The monoclonal antibody is covalently linked to the HCG surface using the maleimide-thiol coupling strategy described in the Methods section. The standard curve for cTnI binding to anti-cTnI on the HCG surface is generated by measuring the change in the resonance wavelength for different dilutions of purified cTnI in PBS (0.1ng/ml to 80μg/ml; Figure 19 (a)). Purified cTnI is also measured after being diluted at 4 defined concentrations in fetal bovine serum on the HCG device. The concentrations of cTnI in the different serum samples are determined by comparing their spectral shifts to the standard curve (black triangles in Figure 19(a)). The concentrations of cTnI recorded on the HCG device are comparable to those that occur in the serum of stroke victims, and to those reported for commercial assays of serum cTnI.

Discussion

Clinical diagnosis of diseased states based on quantitative analysis of biomarkers present in serum require assays that are robust, sensitive, accurate and specific for the target biomarker. These assays are increasingly being carried out using ELISA on POC devices. The ELISA technique however, requires multi-step processing of the sample and detection reagents, which complicates the design of the device. Moreover, since the readout signal is generated using heterogeneous antibody-enzyme conjugates the performance of ELISA's is subject to vendor to vendor, and batch-to-batch variability. In this study we used high contrast grating (HCG) resonator for label-free detection and quantification of interactions between specific antibody-antigen pairs. The low-cost device is simple to construct and allows for sensitive and robust, surface-based detection formats to quantify disease biomarkers in serum within 4 minutes. Our studies show that cTnI can be detected in a mock serum sample with a sensitivity of 100pg/ml, a level of detection that falls within the range of serum cTnI levels associated with stroke (~400 pg/ml is the normal cutoff) [93, 98]. The simple design of the HCG sensor, which is based on a standard silicon manufacturing process, allows for the fabrication of more than10000 unique sensors on a single cm^2 chip complete with integrated microfluidic and electronic systems. The integration of a stand-alone tunable laser and photodiode helps to reduce the cost of the measurement system, while the surface-normal fiber detection format overcomes a requirement in other competing devices for continuous adjustments to maintain a precise optical alignment. A simple extension of the HCG platform described in this study would be to combine a HCG sensor array with a fiber array, as shown in Figure 19(b). This new platform could facilitate high-throughput, parallel screening of biomarkers in thousands of samples. Finally, the HCG label-free biosensor is shown to perform well in mock clinical diagnoses of cTnI in serum, providing both equilibrium and kinetic analyses of the target protein over a concentration range that is relevant for the clinical diagnosis of cardiac infarction.

Material and Methods

Fabrication method

The devices are patterned onto a 6 inch silicon-on-insulator with Si-layer thickness 500nm wafer (from SOITEC) using DUV (ASML 300) lithography followed by silicon refractive ion etching (Lam Research), which are both standard processes in semiconductor manufacturing.

Reflection spectrum measurement

A tunable laser (HP 8164) centered at 1550nm is used as the excitation and is set in a continuous sweeping mode between 1560nm and 1565nm at a rate of 40nm/sec. The power of the reflected light is recorded using a photodiode in real time and is synchronized to the laser sweep rate.

Antibody immobilization

Maleimide groups are introduced to the antibody by treating the antibody (1mg/ml) with 100 uM maleimidobenzoic acid succnimide ester (MBS, Sigma) in PBS for 2hrs at room temperature. The mixture is then passed over a PD-10 column in PBS to remove unlabeled MBS and fractions containing the MBS-antibody conjugate are pooled. The surface of the Si-sensor is thiol-silanized using a fresh 5% solution of (3-Mercaptopropyl) trimethoxysilane (MPTMS) in IPA for 1hr. After washing with PBS the surface is treated with a 1mg/ml of the MBS-antibody. The reaction between the MBS-antibody conjugate and surface thiol groups on the HCG results in a stable thioether bond. After an incubation period of two hours, the surface is washed with PBS, and a blocking buffer containing 3%BSA is applied to the surface to reduce the non-specific binding of serum proteins.

Chapter 4

Dissertation of a novel mitochondrial mediated Necrosis pathway

Introduction

Homeostasis is maintained in multicellular organisms through a balance of cell proliferation and cell death. Programmed cell death is triggered during development and in diseased and damaged tissue and allows the body to eliminate damaged or inappropriately stimulated cells. Three major cellular processes associated with cell death have been described: apoptosis (type 1), cell death associated with autophagy (type 2), and necrosis (type 3) [99-102].

Necrotic cell death has been shown to be the critical regulator of disease pathologies including Alzheimer's, Parkinson's, ischemia-reperfusion, stroke and infection [103]. Recent studies also suggest an important role of necrosis in controlling viral infection and stimulating immuno-surveillance [104, 105]. In addition to its biological importance in pathological cell death, as a tightly regulated cell death pathway, programmed necrosis may exert an anti-cancer function *in vivo*, similar to apoptosis [106]. Necrosis was not characterized as a programmed process until recently as it was originally thought of as an accidental and uncontrolled process, a consequence of extreme physicochemical stresses. While our understanding of the mechanism and regulation of necrosis is still somewhat limited, significant progress has been made over the last decade. The main conceptual change is that necrosis may be considered as a highly regulated cell death pathway, both in its occurrence and in its appearance [107, 108]. Many stimuli including death domain receptors, reactive oxygen species (ROS) and calcium overload have been showed to trigger necrosis leading to defined steps and signaling events that are reminiscent of those characterized for programmed cell death [108].

TNFα (tumor necrosis factor alpha) is a potent inducer of necrosis in many cell types; it is so far, the most characterized necrosis pathway. TNFα normally stimulates a plasma membrane associated complex 1, which triggers activation of NF-κB (nuclear factor kappa-light-chain-enhancer of activated B cells) initiated cell survival response. But when complex 1 is internalized, the cytosolic complex II forms containing RIP1(receptor-interacting protein 1), RIP3 and caspase 8. This complex is considered the pro-death complex. Normally, Caspase 8 will cleave RIP1 and RIP3 and initiate apoptosis, however, in the presence of caspase inhibitors, or in the absent of caspase 8, RIP1 and RIP3 are phosphorylated and forms a necrosome that initiates necrosis [109-112]. A small molecule Nec-1 (Necrostatin-1) was identified that inhibits necrosis by allosteric-blocking of the kinase activity of RIP1. Nec-1 abolishes the assembly of the RIP1-RIP3 complex, suggesting that the kinase activity of RIP1 is required for necrosome formation. Necrosis depends on a tightly-regulated mutual relationship between RIP1 and RIP3 kinase activities, involving the auto-phosphorylation of RIP1 and direct or indirect RIP3 mediated phosphorylation of RIP1. Several other necrostatins have been identified according to their ability to suppress TNF induced necrosis [113, 114]. So far, two RIP3 downstream kinase substrates have been identified to be the positive regulator of

TNF induced necrosis, PGAM5 (phosphoglycerate mutase family member 5) and MLKL (mixed lineage kinase domain-like) [115, 116]. PGAM5, as a protein phosphatase, is activated by RIP3 mediated phosphorylation. Active PGAM5 will dephosphorylate and activate the mitochondria fission factor Drp1 that induces mitochondria fragmentation. Mitochondria permeability and fragmentation has long been associated with necrosis [117]. When necrosis is executed, the mitochondria permeability transition pore is deregulated, leading to an increase in ROS production and calcium imbalance, which eventually cause disintegration of the organelle. The subsequent release of cytotoxic hydrolase and ferrous ion from mitochondria matrix and lysosome further enhances the disruption of membrane integrity and increases ROS production and calcium imbalance [118].

In addition to the death receptor induced necrosis pathway, other chemical stresses, including ROS and calcium-overload can also induce necrosis through the mitochondria pathway. PGAM5 has been found to be an important regulator in both ROS and calcium overload necrosis [119].

In our group's previous study, a small molecule compound, necrocide 1 (NC-1), which is currently under development as an anticancer drug, was identified as an inducer of programmed necrosis in a broad spectrum of human cancer cell lines. Further characterization of NC-1 induced necrosis reveals unique features of this pathway. First, NC-1 induced necrosis independent of caspase inhibitors, second, this pathway does not require TNFR, and finally, necrosome inhibitors cannot completely block necrosis initiation. All together, we believe a novel necrosis pathway is induced by NC-1 and can be utilized as a tool to dissect the general pathway of necrosis.

Results

Confirming NC-1 induces necrosis, not apoptosis or autophagy

Cleavage of PARP(Poly (ADP-ribose) polymerase) and caspase 3 are widely used as markers for the activation of the apoptosis pathway [120]. The LC-II (Microtubule-associated proteins 1A/1B light chain 3) complex is formed when LC3 is recruited to the autophagosomal membranes during autophagy and is therefore a potent marker for autophagy [121]. On the other hand, no specific marker has been identified for necrosis. Since none of the apoptosis or autophagy markers are detected during necrosis [117], researchers have had to use an elimination method to distinguish necrosis cell death. More recently however, release of the intracellular protein CyPA(Cyclophilin A) from cytosol has been identified as a marker for early necrosis [122].

In order to affirm the cell death induced by NC-1 results from necrosis, the biological markers PARP, caspase 3, LC-II, and CyPA were tested for apoptosis, necrosis and autophagy. MCF-7 cells were treated with NC-1 and the apoptosis inducer TNFα for various lengths of time, the supernatant growth medium and cell lysate was collected separately for Western blot assays. As shown in Fig.20, formation of the LC3-II complex did not occur in both TNFa and NC-1 treatments, eliminating the possibility of

autophagic pathway activation. Cleaved Parp and Caspase 3 can be detected after 3 hours of TNFa treatment suggesting onset of apoptosis, but is not detected with NC-1 treatment even after 24-hours, which indicates NC-1 does not induce apoptosis in treated cells. Moderate amounts of CyPA were detected in the supernatant of TNFa treated cells following a 3 hour treatment; this is most likely due to leakage of the cell contents from already-dead cells, the level of CyPA notably increased at 24 hours when majority of cells are dead or have impaired cell membranes. Significantly higher levels of CyPA were observed in NC-1 treated cells at 3 hours compared to TNFa treated cells, suggesting the onset of necrosis. In our previous studies, florescent images (Fig. 20C) of NC-1 induced cell death showed a swelling of the nucleus and fragmentation of chromosomes along the nucleus membrane, which morphologically resembles necrotic cell death. The combination of morphological assembly and release of necrosis biomarkers, it our studies suggest that NC-1 induces necrosis in treated cells.

Characterization of NC-1 induced necrosis.

To gain insight into the mechanism of action of this novel necrosis pathway, a kinome screen was conducted by our colleague Christina Trojel-Hansen. The screen involved knocking down 691 human kinases using small interference RNA in individual cells. The screen identified 16 kinases that conferred significant protection against cell death induced by NC-1 with the notable inclusion of RIP4, a member of the RIP family of kinases. Other RIP family kinases including RIP1 and RIP3 have been characterized as important regulators of TNF- and zVAD- induced necrosis, that form necrosomes upon activation [123]. Significantly, RIP4 had not been previously linked to necrosis signaling. RIP kinases share a similar kinase domain, yet they are also characterized by shared capacities to transmit intracellular responses to various environmental factors [124]. In the past few years, progress has been made towards understanding the functions of different RIP family members. RIP4 was identified as an important component in the NF-kB pathway and is a substrate of caspase in apoptosis [125-129]. RIP2 was also implicated in the NF-kB pathway and apoptosis [130]. The function of RIP5,6 and 7 were largely unknown, but RIP5 shares more than 30% sequence similarity with RIP4 [131], This high resemblance in overall structural organization suggests a function similar to that of RIP4 [132]. RIP7 and RIP6 also share high sequence similarity and missense mutations of RIP7 have been identified in several major neurodegenerative diseases associated with Parkinson's disease [133-135].

To further confirm the involvement of RIP4 in the protection of NC-1 induced necrosis, RIP4 was knocked down by transient transfection of siRNA. As shown in Fig.21, the high efficiency of the RIP4 knock-down was confirmed by western blot analysis. The cell survival rate in RIP4 KD cell increased by 20% in the knock-down compared to transfection with a mock siRNA. We further analyzed whether RIP4 KD reduces necrotic cell death by recording the release of CyPA. MCF7 WT and RIP4 KD cells were treated with 25nmol of NC-1, as shown in Fig.21, RIP4 KD cells release significantly less CyPA compared to WT. Our studies suggest that RIP4 is a positive regulator of NC-1 induced necrosis.

In the RIP1, RIP3 studies, necrostatin-1 was found to interact directly with RIP1 to inhibit its kinase activity. Next we considered the possibility that NC-1 may also function to interfere with RIP4. To test this hypothesis, an *in vitro* kinase assay was conducted using overexpressed and tandem affinity-purified RIP4. In our assay, purified RIP4 was incubated with p35-labled ATP and phosphorylation by was measured by autoradiography. As shown in Fig.22, the level of phosphorylation of RIP4 decreased in the presentce of NC-1, indicating a direct effect of NC-1 on RIP4 kinase or its interacting partners. RIP1 and Nec-1 was also included in the assay as a positive control. As shown in Fig.22, RIP1 auto-phosphrylation decreased significantly in the presence of Nec-1, which is consistent with our previous studies, but did not change with NC-1.

Identification of the RIP4 complex

In order to identify the RIP4 complex with NC-1 treatment, tandem affinity purification was used to pull down proteins that interact with RIP4. An inducible RIP4-FLAG overexpression cell line was established with MCF-7 cells. RIP4 expression was induced by doxycycline before incubation with NC-1 and the collection of cell lysate. Tandem affinity purification coupled with mass spectrometry was carried out on the RIP4 pull-down with the main components being identified as Mule and PGAM5l (Fig.22). PGAM5 is a phosphatase that is located on the outer membrane of mitochondria and has been previously reported as a positive regulator of both TNFa and ROS induced necrosis through its activation of the mitochondria fission factor Drp-1 [136]. Mule is an E3-ligase that has reported to positively regulate apoptosis by degradation of Mcl-1 and HDAC2 [137] [138], but was not previously linked in necrosis pathway.

Discussion

Previous studies of the necrosis pathway were mainly based on analysis of membrane receptor induced pathways, which overlap largely with apoptosis. NC-1 is the first compound that has positively been identified with the induction of necrosis without apoptosis inhibition. The identification of NC-1 provides an unprecedented opportunity to broaden our understanding of the molecular regulation of necrosis.

We also identified a new necrosis regulator RIP4 and its necrotic complex components, PGAM5 and Mule. PGAM5 is a mitochondria localized phosphatase. Mitochondria fragmentation has been implicated in necrosis for many decades, but only recently, has a necrosis induced mitochondria fission pathway been described. In this pathway PGAM5 was shown to be activated by RIP3, which in turn activates a downstream target, Drp1. Active DRP1 subsequently localizes to the mitochondria and induces fission[136]. Since PGAM5 was found in the NC-1 induced RIP4 necrotic complex, we propose that RIP4 induces necrosis through our newly discovered PGAM5 mediated mitochondria pathway. A deterioration of mitochondrial health has been implicated in many stress response and cell death pathways such as mitophagy and intrinsic apoptosis, with permeabilization of the outer mitochondrial membrane being a signature event in the onset of intrinsic apoptosis [139]. It is reasonable to speculate therefore that

RIP4 induces necrosis by altering PGAM5 and DRP1 function and a consequence of this activity is mitochondrial fragmentation.

The identification of the TNF-independent necrosis inducer NC1 provides an opportunity to broaden our understanding of the molecular regulation of necrosis. Once regulation is clarified, these studies could provide us with more defined knowledge of necrosis and its execution. With an increased implication of necrosis in human disease, a deeper understanding of necrosis will provide considerable insight on disease pathology and may provide new targets for drugs that could be used to interpret the disease pathologies and to provide more specific targets for anti-cancer drug and pathologic necrosis

Material and Method

Preparation and maintenance of cells

All cells used were provided by UC Berkeley Tissue Culture Facility. Cells were cultured in high- glucose DMEM with GlutaMAX (Life Technologies, cat. 10566-016) supplemented with 10% FBS (Life Technologies, cat. 16000-085) 1% Penicillin/Streptomycin Solution (Life Technologies, cat. 15140-122) in humidified 5%CO_2 incubator at 37 degree Celsius. Cells were passaged at confluence.

SiRNA for human RIP4 and mock were purchased from Santa Cruz and transfected MCF-7 cells according to the manufacturer's protocol.

Cell survival assay was performed using SYTOX® Green Nucleic Acid Stain (Molecular Probe) according to the manufacturer's protocol and analyzed by Flow cytometry.

Tandem affinity purification

293T cells were cultured in DMEM supplemented with 10% FBS. When the cell confluency rises to 80-90%, cell transfection was performed using PEI solution (30μg/15cm dish). Two days after transfection, whole-cell lysates (WCLs) were prepared in tandem affinity purification (TAP) buffer [20 mM Tris HCl (pH 7.5), 150 mM NaCl, 0.5% Nonidet P-40, 1 mM NaF, 1 mM Na_3VO_4, 1 mM EDTA, protease inhibitor mixture (Roche)], recombinant proteins were pulled down using anti-flag beads. Before elution, the beads with recombinant proteins were given three washes using high salt buffer [20 mM Tris HCl (pH 7.5), 650 mM NaCl, 0.5% Nonidet P-40]. The proteins were finally eluted using flag peptide solution and analyzed by SDS-PAGE.

Silver staining was preformed using the Pierce™ Silver Stain Kit (Thermo Scientific) according to manufacture's protocol, each protein band was cut off and analyzed by Mass spectrometry.

In vitro kinase assay

Recombinant FLAG-RIP4 protein was purified from transfected HEK293T cells as previously described in tandem affinity purification. Kinase reaction was initiated by addition of 10 mM cold ATP and 1 mCi of [g-32P]ATP, and reactions were carried out for 30 min at 30 1C. Reactions were stopped by boiling in SDS-PAGE sample buffer and subjected to 8% SDS-PAGE. Protein band was visualized by analysis in a Storm 8200 Phosphorimager.

Figures

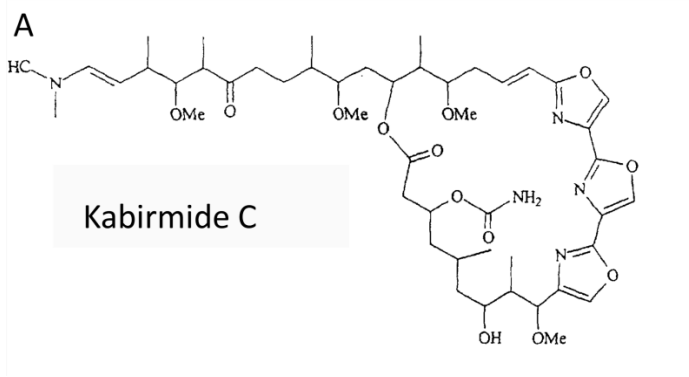

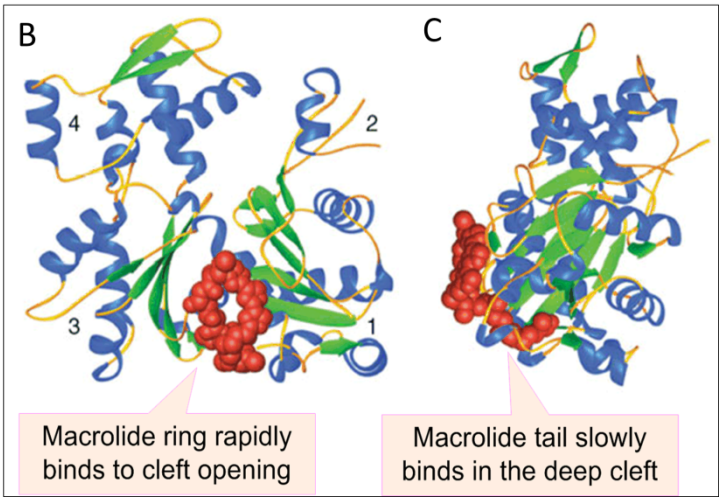

Figure 1. Kabiramide C structure and Actin-binding mechanism. A. The chemical structure of Kabirmide C with a macrolide ring and tail. B. First step of KabC-actin binding mechanism involving the rapid interaction of macrocyclic ring of KabC with residues at the entrance of the cleft between SD1 and 3 at the barbed-end of actin protomer. C. the second step of KabC-actin binding when the macrolide tail penetrates into the SD1, SD3 cleft to form a strong and long-lived KabC-actin complex.

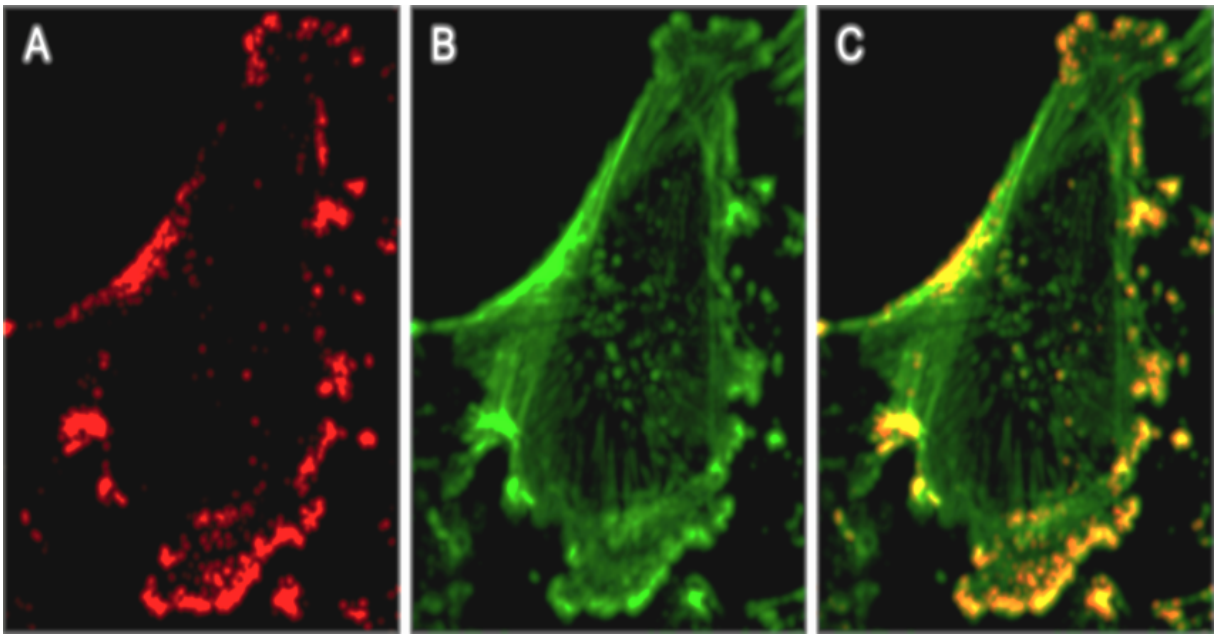

Figure 2. Selectivity of the binding of fluorescent KabC to the barbed ends of actin filaments in fixed mammalian cells. A. TMR-KabC staining in fixed NIH 3T3 cells represented by the red color. B. FITC-phalloidin staining in same cell represented by the green color. C. overlay image of TMR-KabC and FITC-phalloidin.

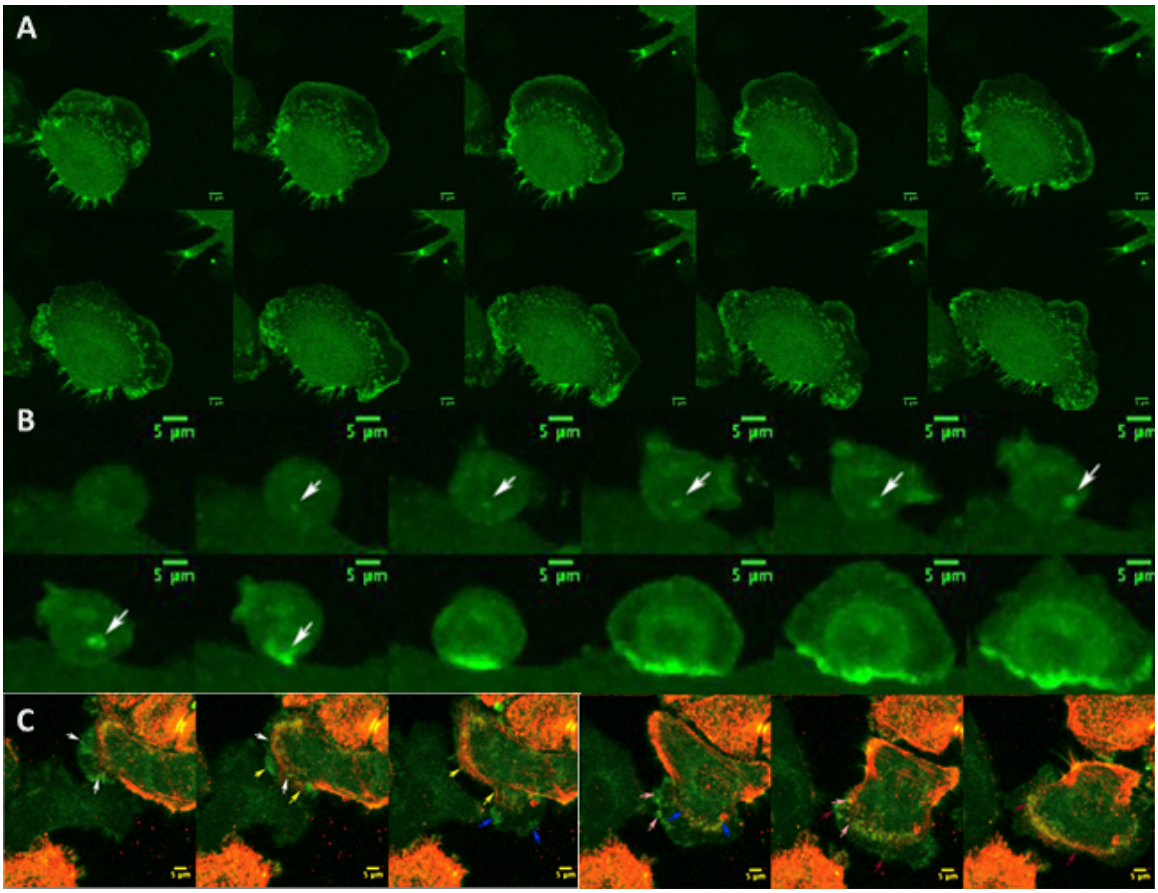

Figure 3. Generation of free barbed ends during movement and cell spreading. A. motile cell with lamellipodia formation. Live NBT-II cells stained with SiR-KabC, images were taking every two minutes. B. Cell attaching to surface. A live NBT-II cell stained with SiR-KabC attaching to the surface of culture plates after trypsin digested. White arrow pointing to the KabC cluster formed and grew as cell attached and spreading. Images were taking very 4 minutes C. SiR-Jas and TMR-KabC co-staining of motile cells. The position of arrows with same color remain stationary in two consecutive frames, and the arrows point to TMR-KabC clusters first in the first image, and in the second image SiR-Jas staining, which representing actin filaments, move to the arrow position.

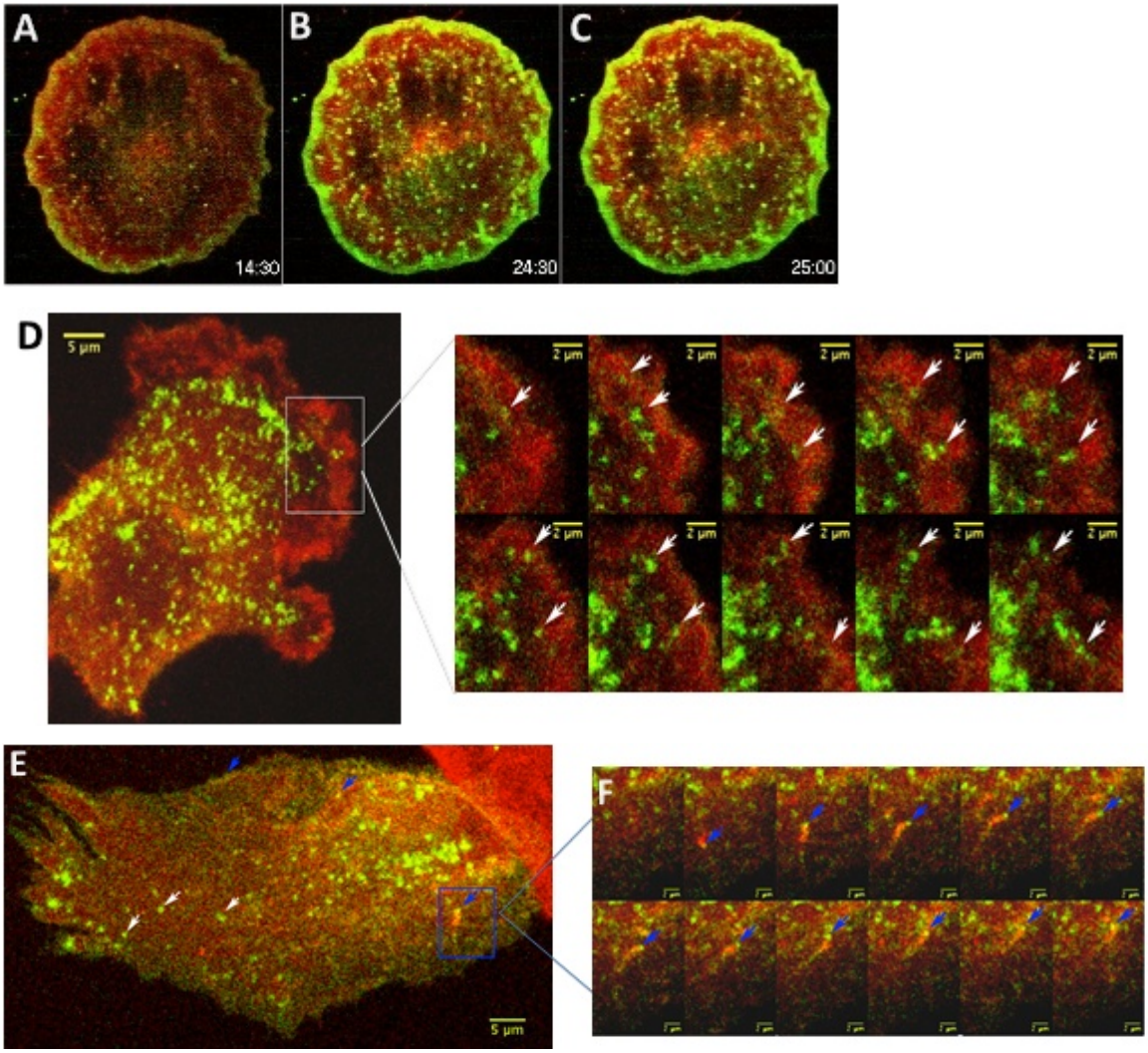

Figure 4. Generation of free barbed ends during PDGF-mediated endocytosis. A-C. PDGF-induced endocytosis in Rac-1-GFP transfected Hela cells staining with TMR-KabC. A. Before PDGF addition. B-C. two consecutive frame of TMR-KabC and GFP fluoresce image of the cell after adding PDGF. D. SiR-KabC staining of Fyve domain-GFP expressing Hela cells demonstrate generation of endosome from the barbed-end rich plasma membrane. White arrows point to the endosome generation site. E. Two pools of endosomes existed in PDGF-induced endocytotic Hela cells. White arrows indicate the pre-exist, stationary endosomes, blue arrows indicate the endosome generated after PDGF induction. F. close-up montage of one endosome generated close to plasma membrane

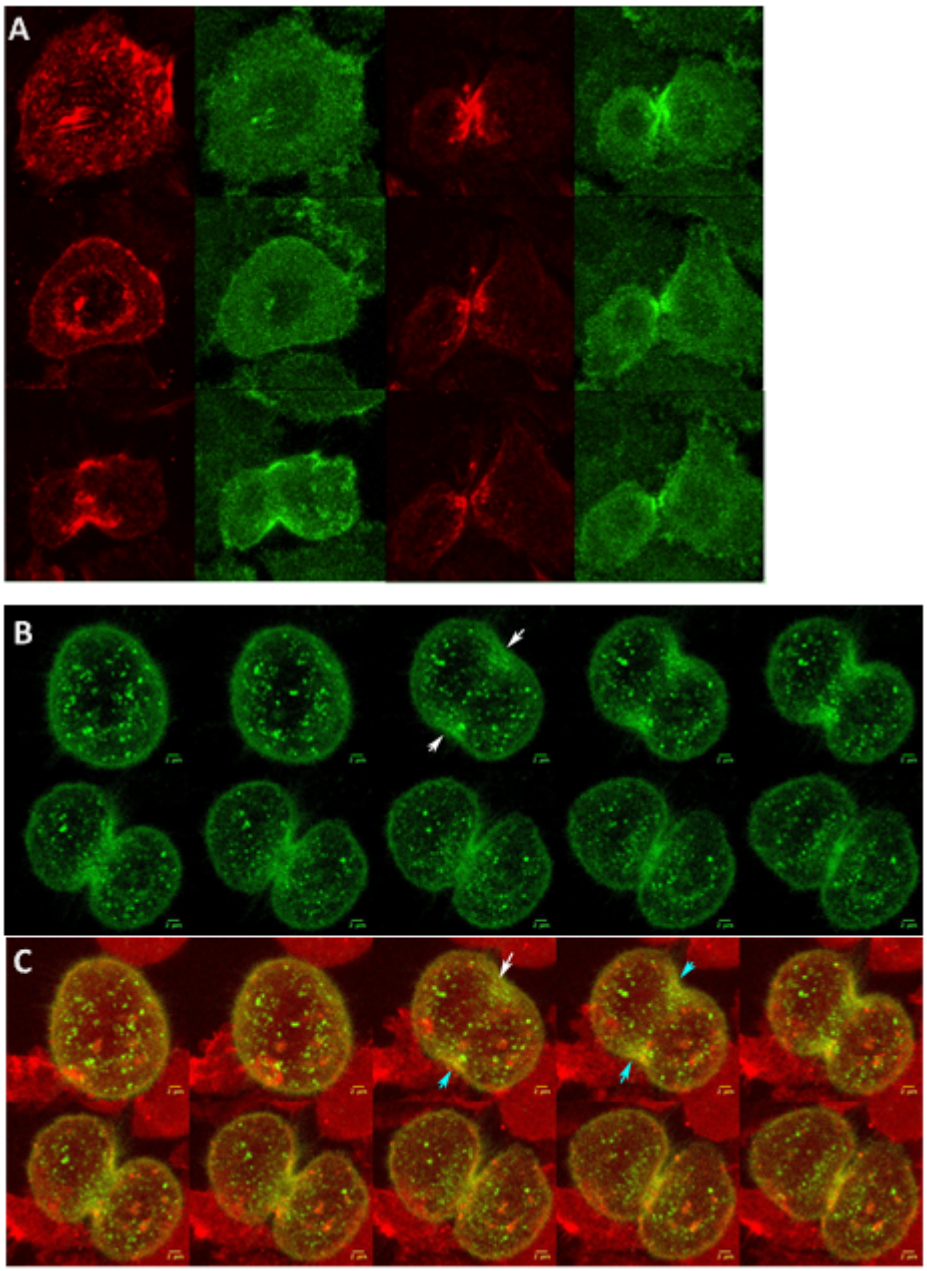

Figure 5. Generation of free barbed ends during cytokinesis. A. SiR-Jas (Red) and TMR-KabC (Green) double staining of NBT-II cells undergone cytokinesis. B-C. Correlation of endosome movement and actin filament propulsion during cytokinesis. B. GFP fluorescent image of FYVE domain-GFP expressing Hela cell during cytokinesis. Arrow showed the movement of endosome towards cleavage furrow at the on set of cytokinesis. B. overly of FYVE domain-GFP image with SiR-KabC images. Arrow indicates movement of endosome not associated with new barbed end formation.

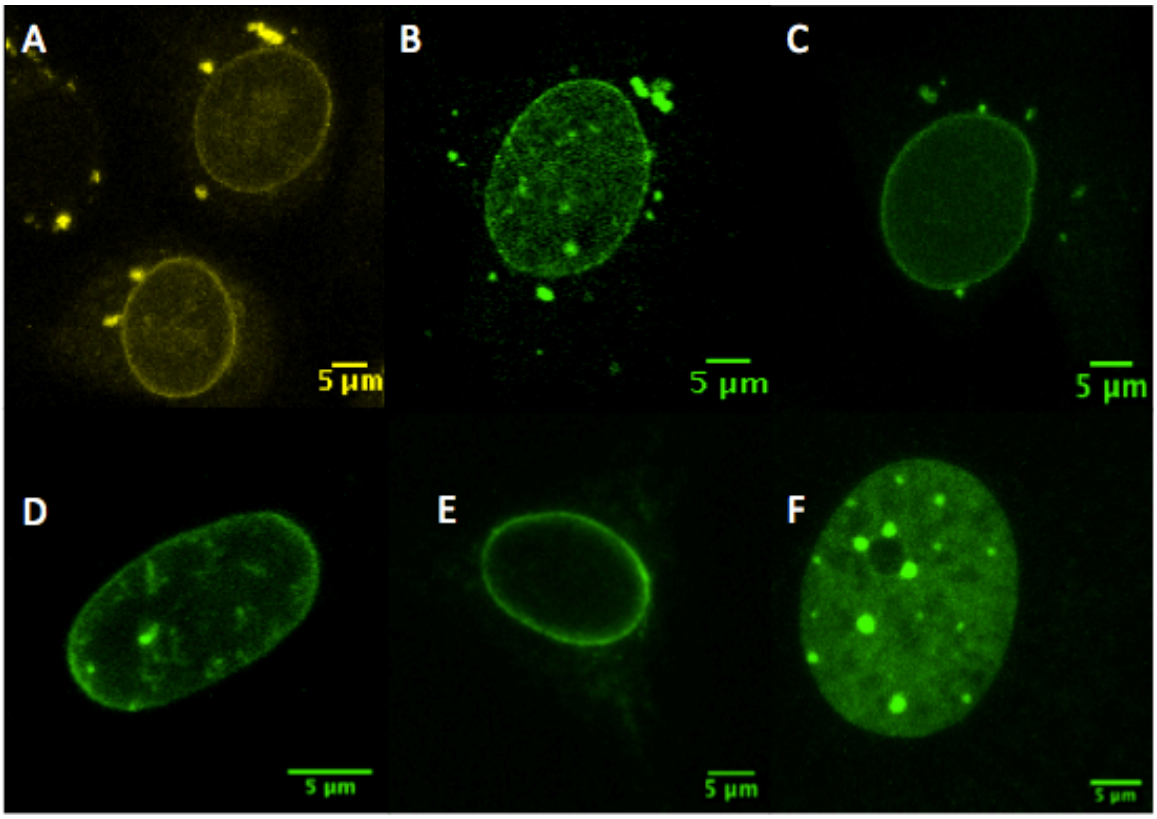

Figure 6. Visualization of nuclear proteins. A-E, Emerin-YFP, Sun1-GFP, Sun2-GFP, LaminA-GFP and Nesprin2-mini-GFP were transiently expressed in NIH 3T3 cells, fluorescent images were taking with live cells using Zeiss 710 confocal microscope with an environmental chamber for the live visualization of nuclear membrane. F. Ear fibroblast cells from Histone 2B-GFP transgenic mice were imaged with same set-up as A-E.

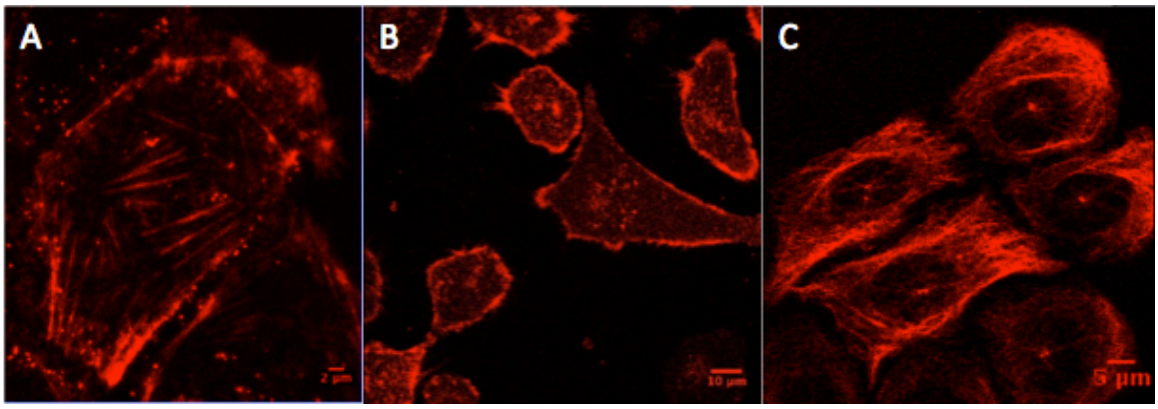

Figure 7. visualization of cytoskeleton component in live cells using SiR conjucated dyes. A. NBT-II cells treated with 10nM SiR-Jas showed strong florescent labeling at the stress fiber and focal contacts. B. NBT-II cells treated with 10nM TMR-KabC showed differential label at barbed end actin at site of membrane protrusion. C. NBT-II cells stainted with 10nM SiR-Texal showed microtubule network.

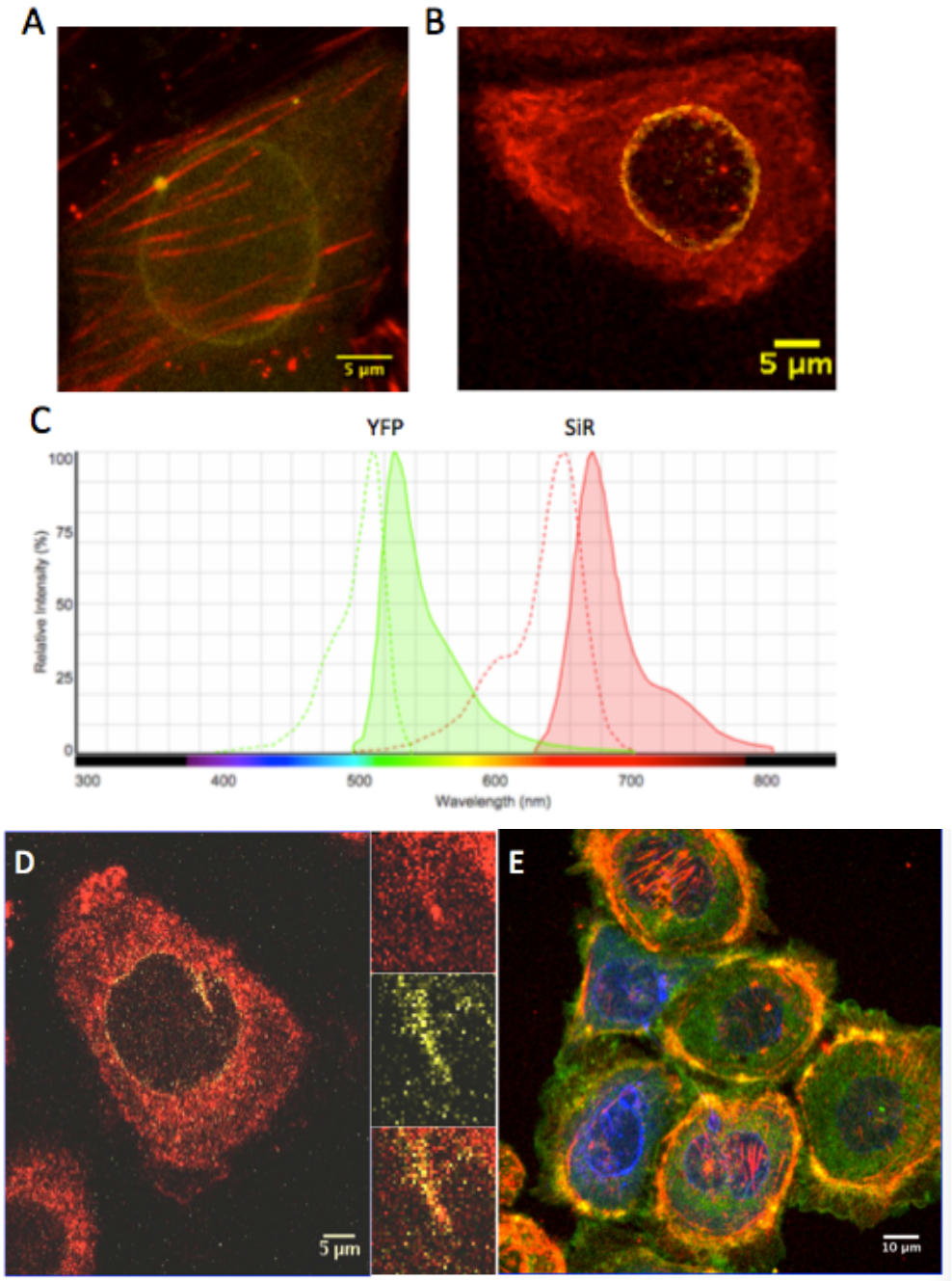

Figure 8. Multicolor imaging of nucleus and cytoskeleton. A-B, Emerin-YFP transfected cells were stained with SiR-Jas and SiR-tub respectively. C. Excitation and emission spectra of SiR and YFP to allow spontaneous imaging of the two dyes. D. Emerin-YFP transfected cells were stained with TMR-KabC, nuclear invagination was observed with localization of intensive KabC staining at the bottom. E. Triple live cell staining of Emerin-YFP, TMR-KabC and SiR-Jas.

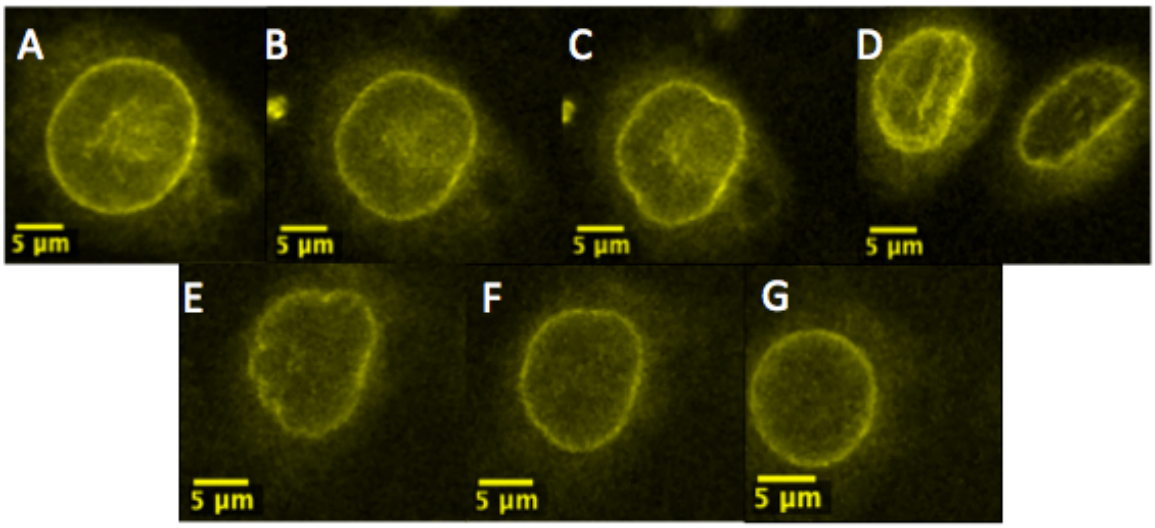

Figure 9. Nuclear response to 5nM blebbistatin treatment. A. Emerin-YFP fluorescent image before addition of blebbistatin. B-F. Emerin-YFP fluorescent images taking every 20 minutes after addition of 5nM of blebbistatin. G. Emerin-YFP fluorescent after 2 hours of blebbistatin treatment.

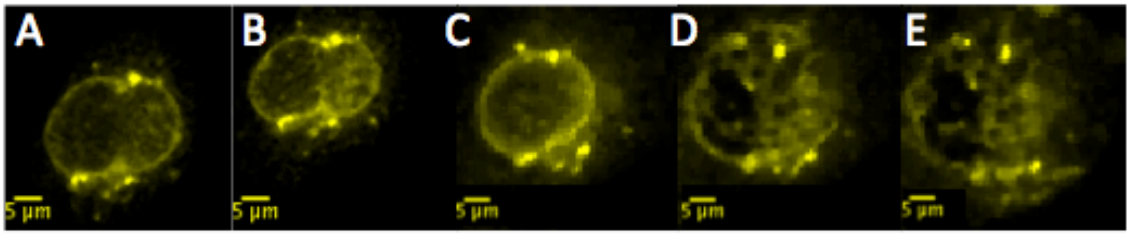

Figure 10. Nuclear response to 10nM blebbistatin. A. Emerin-YFP fluorescent image before 10nM of blebbistatin treatment. B-C. Emerin-YFP fluorescent 20 min and 40 min after addition of 10nM of blebbistatin respectively. D. Emerin-YFP labeled membrane explosion after 1 hour of 10nM blebbistatin treatment. E. Emerin-YFP fluorescent image of interconnected nuclear membrane fragments after the explosion.

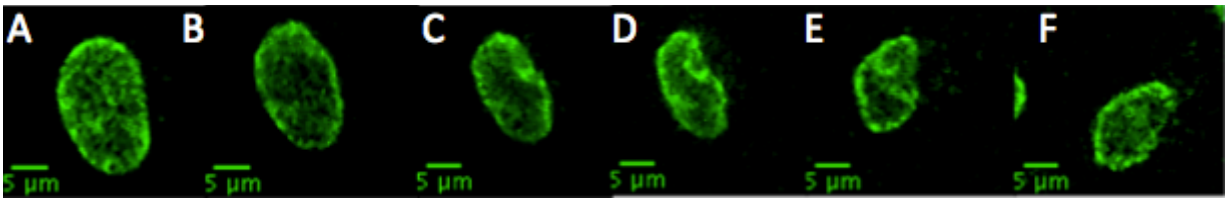

Figure 11. Nuclear response to 5nM of Cytoclasin D treatment. A. Sun2-GFP fluorescent image before 5nM Cyto D treatment. B-E. Images of Sun2-GFP labeled nuclear responding to 5nM CytoD treatment taking every 20min. F. image of Sun2-GFP fluorescent image after 2 hours of CytoD treatment.

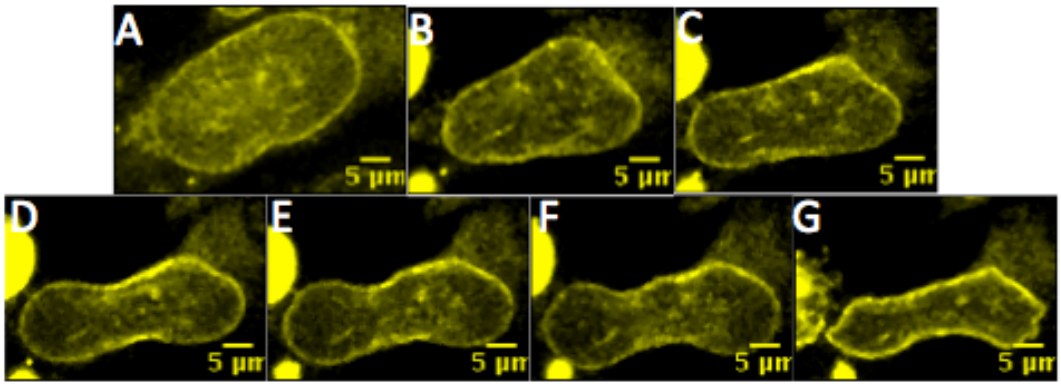

Figure 12. Nuclear response to ROCK inhibitor Y-27632. A. Emerin-YFP fluorescent image before Y-27632 addition. B-F. Emerin-YFP images taking every 20mins after addition of Y-27632. F. Emerin-YFP images taking 3 hours after Y-27632 treatment.

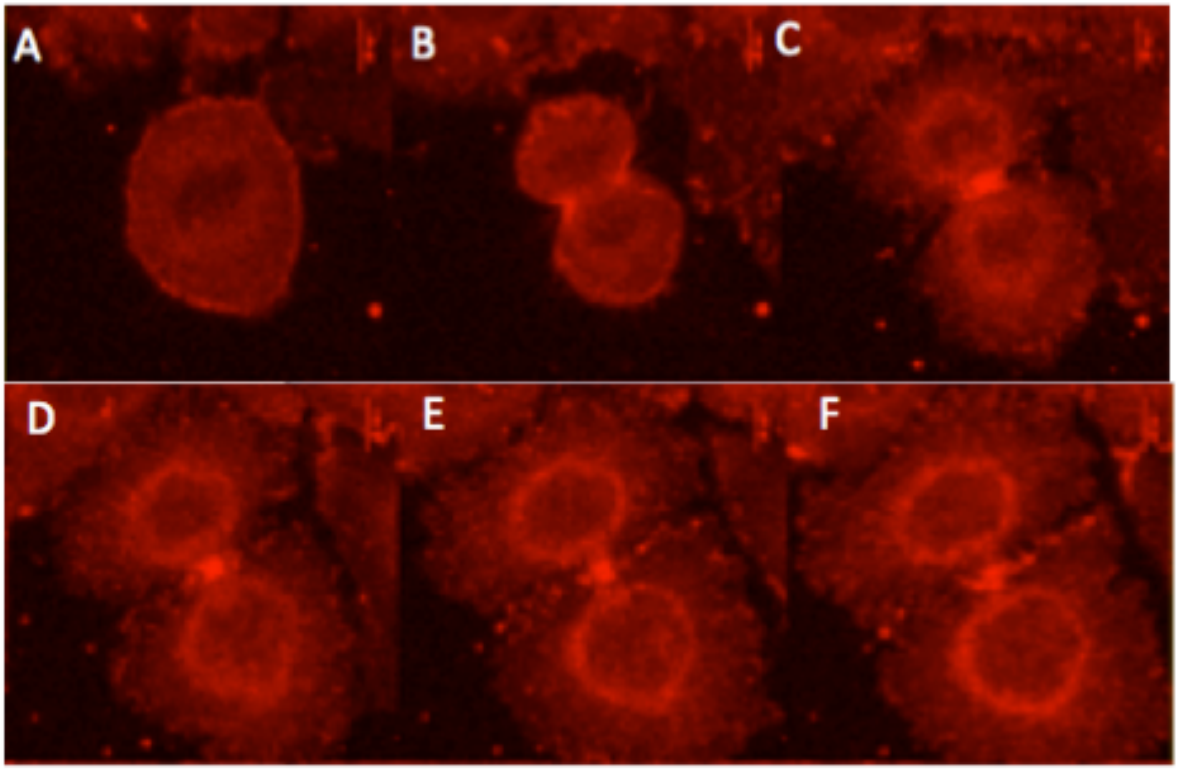

Figure 13. SiR-KabC fluorenscent image of NBT-II cell during cell division. Images were taking very 4 minutes. Two daughter cells separated completely after 20 minutes in F.

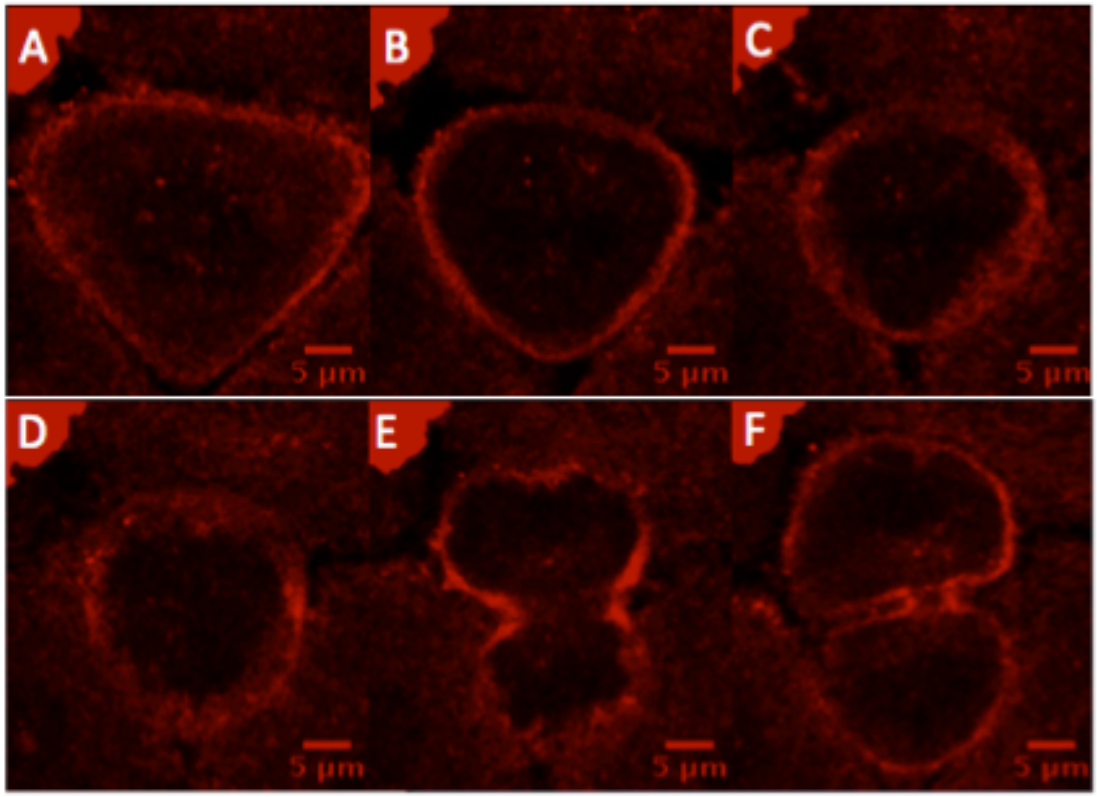

Figure 14. SiR-KabC fluorenscent image of NBT-II cell treated with Y-27632 during cell division. A-E. SiR KabC images taking every 2 minutes. F. SiR-KabC image taking after 2 hours from A, the two daughter cells were still interconnected.

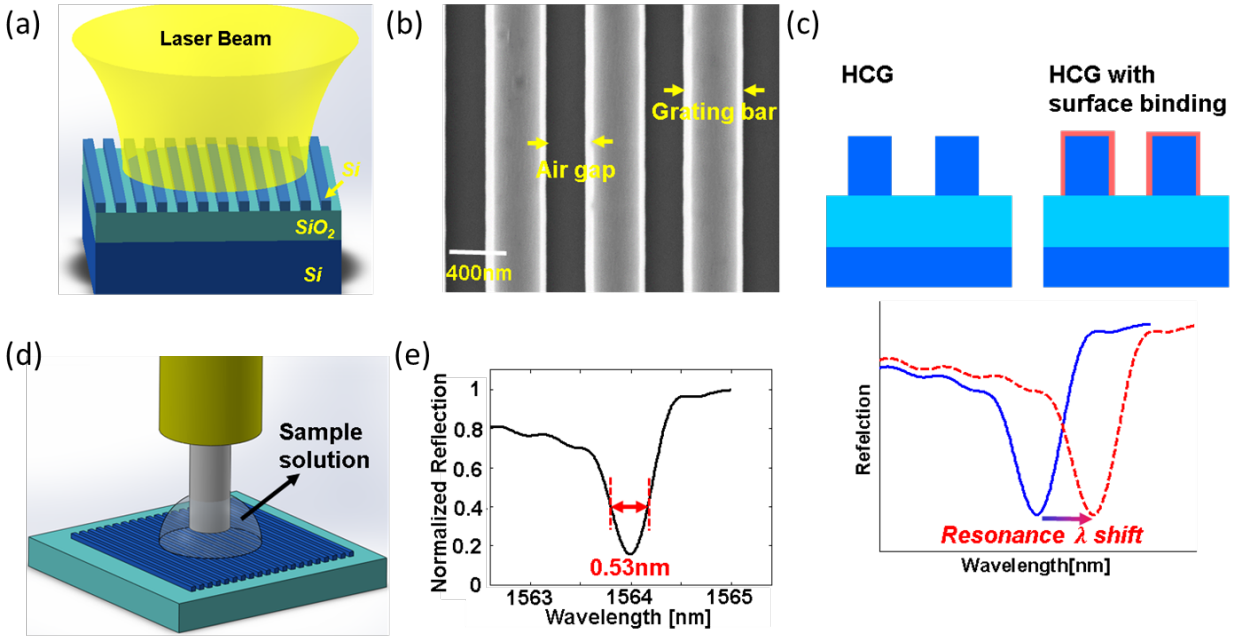

Figure 15. HCG resonator as a label-free biosensing platform. (a) Schematic of a surface normal coupled HCG resonator. (b) SEM image of gratings within a single fabricated HCG resonator. (c) Schematic of the principle of using HCG resonator as a protein binding sensing platform. The red-dashed curve indicates a red-shift in the resonance wavelength occurs when a protein binds to HCG surface. (d) A single mode fiber probe is immersed in the fluid above the HCG surface to avoid surface reflections. (e) A reflection spectrum recorded for a device having the configuration schematized in (d). A tunable laser centered at 1550nm is used as excitation source and is run in a continuous sweeping mode. The reflection power is recorded in real time and is synchronized to laser sweeping rate.

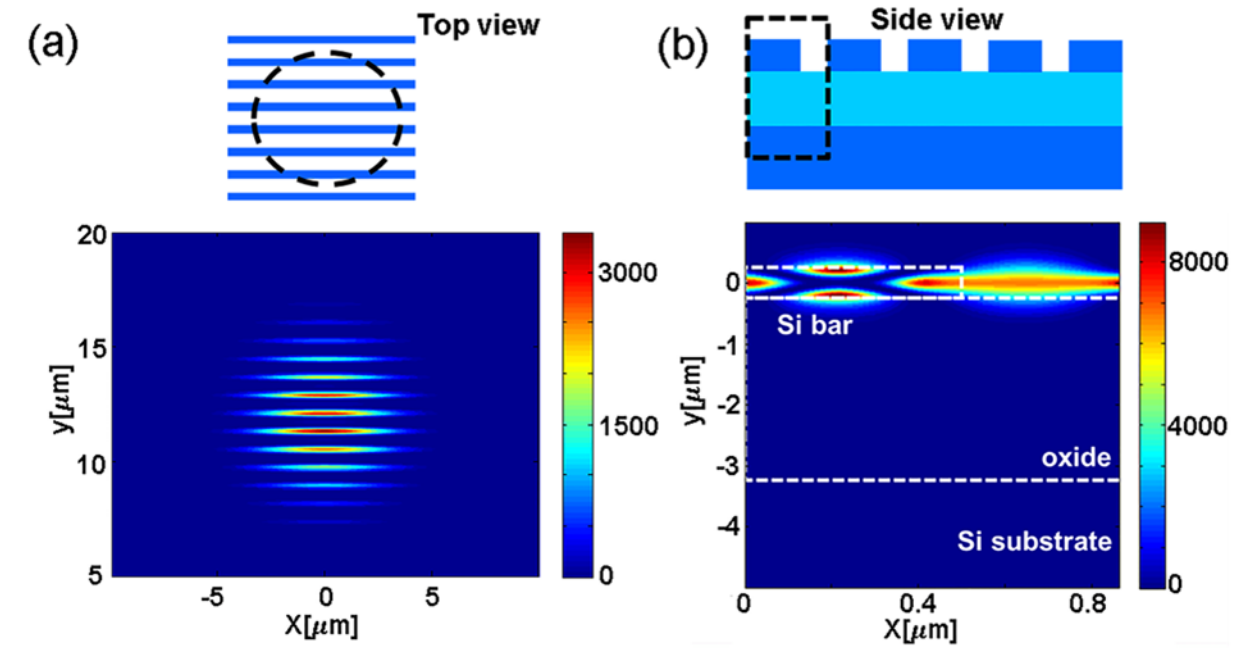

Figure 16. HCG resonator intensity pattern at resonance wavelength. (a) Top view of the resonance inside the HCG cavity excited by Gaussian beam with a 10μm spot size at resonance wavelength (1564nm). A large mode overlap with the input beam contributes to a simple and efficient coupling of the input light. (b) Side view of the resonance (showing one period) inside the HCG cavity. The resonance is designed to have large mode exposure to surroundings, which contributes to the high sensitivity of the device.

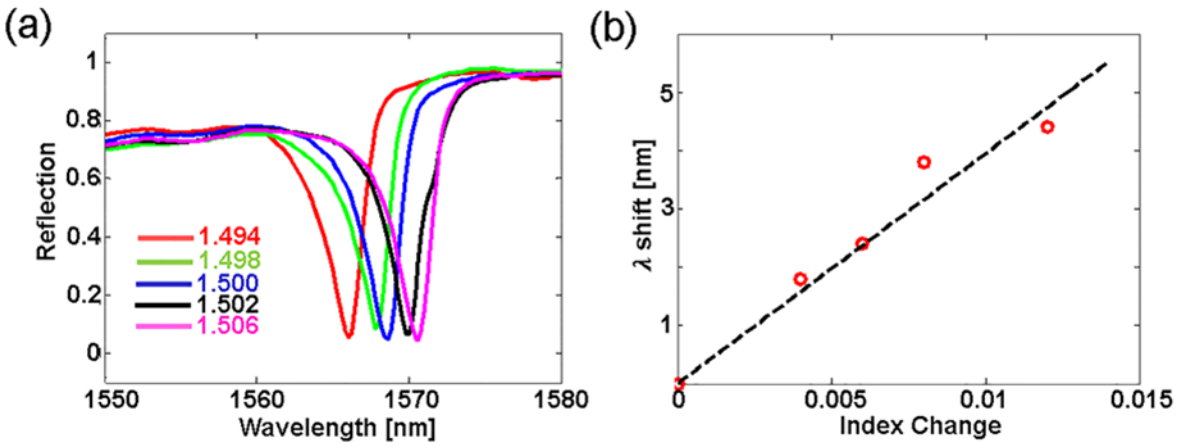

Figure 17. Quantification of HCG sensor sensitivity at different refractive indices. (a) Reflection spectra for a HCG resonator immersed in liquids with different refractive indices ranging from 1.494 to 1.506. (b) Resonance wavelength as function of the change in refractive index.

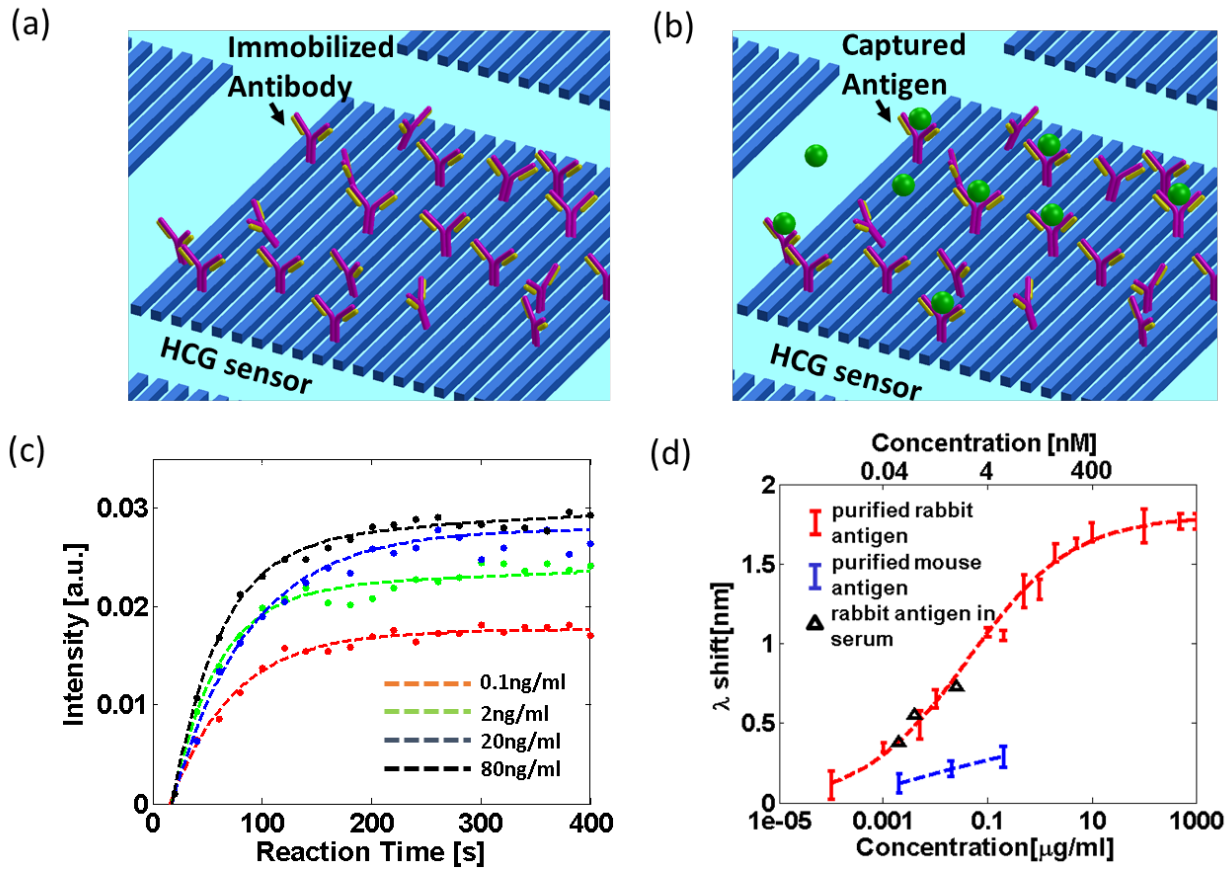

Figure 18. Three-dimensional schematic (not drawn to scale) and the experimental measurements illustrate the detection scheme using HCG resonator as platform for antibody-antigen binding assay. (a) HCG sensor immobilized with capturing antibody. (b) Antigen attaches to the antibody immobilized sensor and changes the surface properties of HCG sensor. (c) Real time recording of the interaction between surface bound goat anti-rabbit IgG and different concentrations of antigen (rabbit IgG). The dashed lines are the corresponding fits to data. (d) Red dots show the resonance wavelength shift for different concentrations of purified rabbit IgG added to a HCG resonator surface-coated with anti-rabbit IgG. The red dashed line is the fit to recorded data. Blue dots show that the incubation of mouse IgG with surface linked anti-rabbit IgG results in smaller shift of the resonance wavelength. The black triangles show the response of the HCG sensor to the addition of rabbit IgG dissolved in goat serum (Sigma). The bars indicate the error range for the 3 measurements.

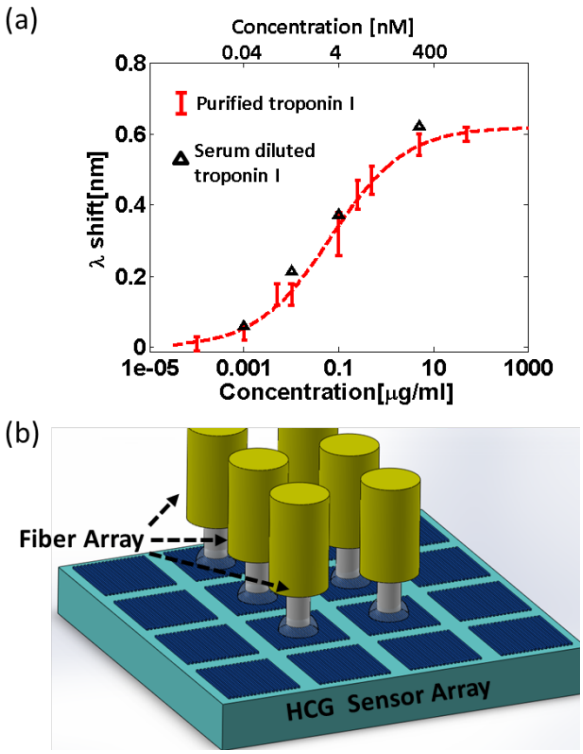

Figure 19. (a) Measurement results for troponin I molecule inside PBS (red dots) and serum (black triangles). The bars indicate the error range over 3 measurements. (b) HCG sensor array combined with fiber array for high throughput screening.

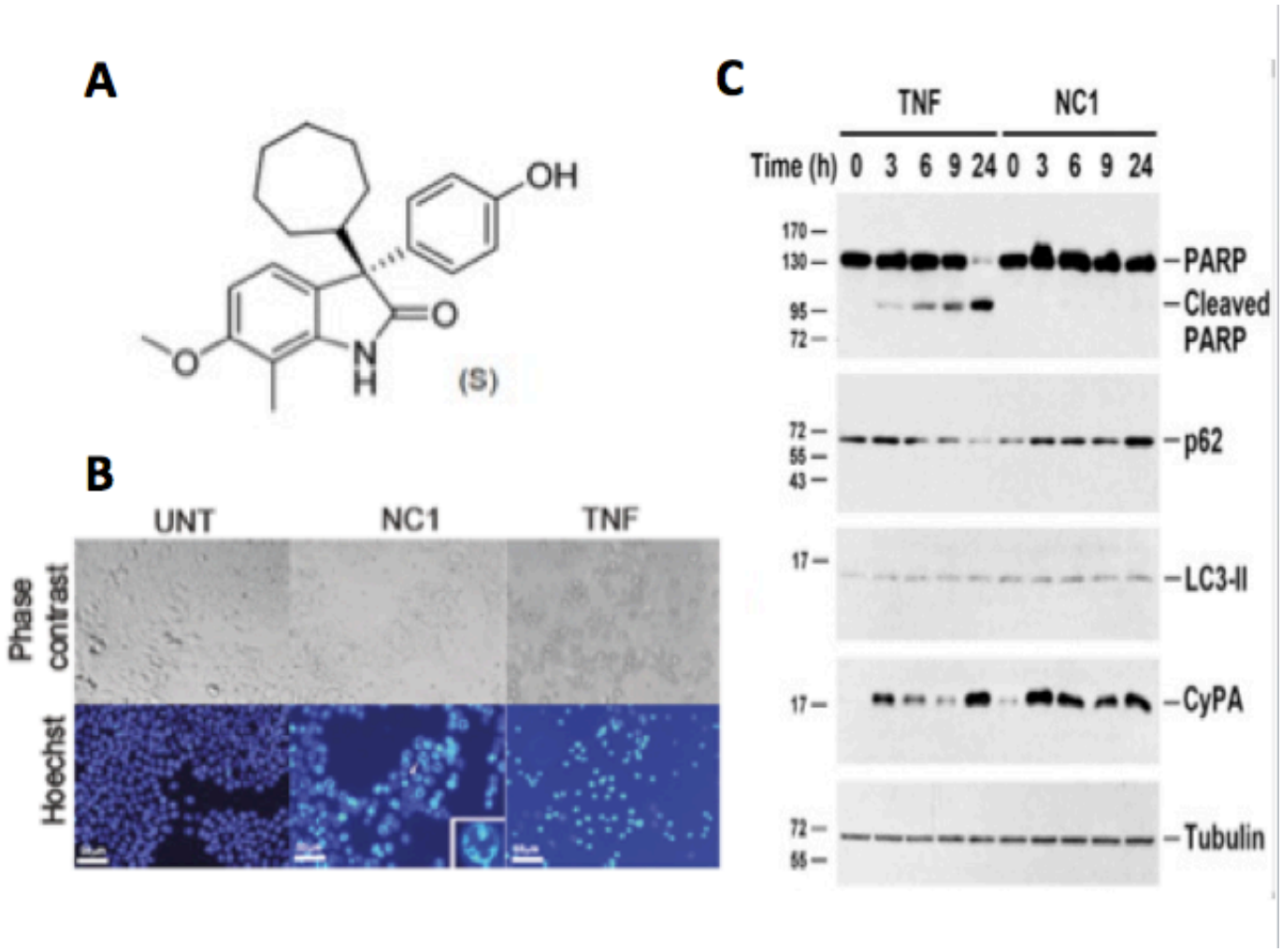

Figure 20. NC-1 induces necrosis. A. The chemical structure of NC-1. B. MCF7 cells were incubated with TNF or NC1 for indicated length of times, then the cell lysate and medium supernatant were collected for western blot detection of necrosis marker CyPA, apoptosis marker cleaved PARP and autophagy marker LC3-II. C. Cells were treated with NC1 and TNF before stained with Hoechst dye for DNA.

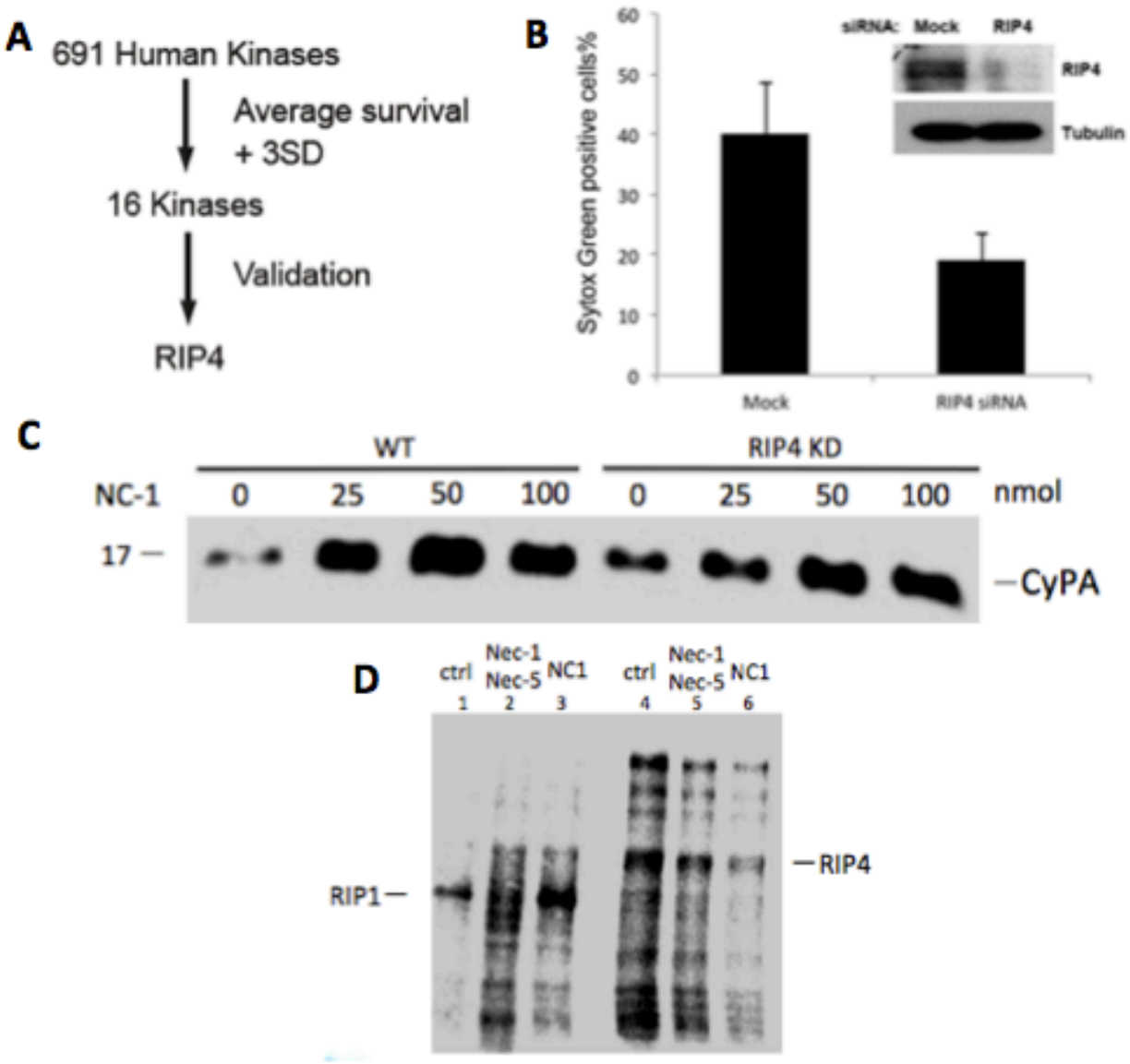

Figure 21. RIP4 is a positive regulator of NC-1 induced necrosis. A. human kinome screening identified RIP4 as a putative regulator of NC-1 induced necrosis pathway. B. RIP4 was knocked down by siRNA, cell survival rate in Mock knock down and siRNA knock down was determined by Sytox Green staining and cell counting. C. Wildtype and RIP4 KD cells were treated with indicated concentration of NC-1, the medium supernatant was collected and CyPA release was detected by Western blot. D. in vitro kinase assay of RIP4 and NC-1. RIP1 and RIP4 was purified from MCF7 cells by immunoprecipitation, then incubate in vitro with radiolabeled ATP and Nec1+Nec5 or NC1. The level of phosphorylation was determined by autoradiography.

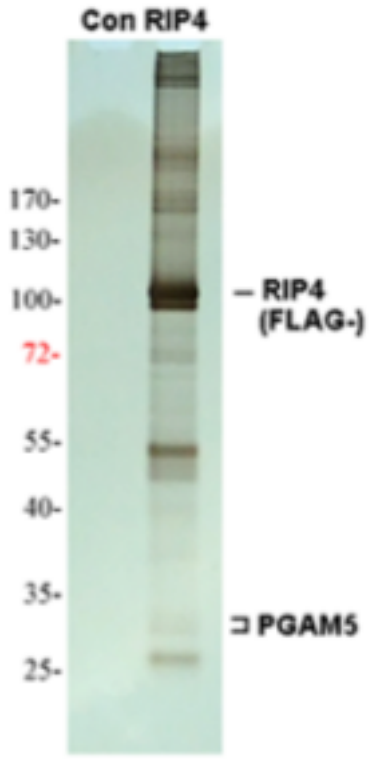

Figure 22. Identification of RIP4 necrotic complex. MCF-7 cells inducible expressing FLAG-RIP4 were treated with NC-1. Cell lysate was collected and RIP4 complex was tandem affinity purified and analyzed on a silver-stained SDS-gel. The bands were cut out and analyzed by Mass spectrometry.

References

1. Theriot JA, Mitchison TJ, Tilney LG, Portnoy DA. The rate of actin-based motility of intracellular listeria monocytogenes equals the rate of actin polymerization. Nature 1992 May 21;357(6375):257-60.

2. Marchand JB, Moreau P, Paoletti A, Cossart P, Carlier MF, Pantaloni D. Actin-based movement of listeria monocytogenes: Actin assembly results from the local maintenance of uncapped filament barbed ends at the bacterium surface. J Cell Biol 1995 Jul;130(2):331-43.

3. Ward BM, Moss B. Vaccinia virus intracellular movement is associated with microtubules and independent of actin tails. J Virol 2001 Dec;75(23):11651-63.

4. Cudmore S, Cossart P, Griffiths G, Way M. Actin-based motility of vaccinia virus. 1995.

5. Silacci P, Mazzolai L, Gauci C, Stergiopulos N, Yin H, Hayoz D. Gelsolin superfamily proteins: Key regulators of cellular functions. Cellular and Molecular Life Sciences CMLS 2004;61(19-20):2614-23.

6. Narita A, Takeda S, Yamashita A, Maeda Y. Structural basis of actin filament capping at the barbed-end: A cryo-electron microscopy study. Embo j 2006 Nov 29;25(23):5626-33.

7. Mullins RD, Heuser JA, Pollard TD. The interaction of Arp2/3 complex with actin: Nucleation, high affinity pointed end capping, and formation of branching networks of filaments. Proc Natl Acad Sci U S A 1998 May 26;95(11):6181-6.

8. Wear MA, Yamashita A, Kim K, Maéda Y, Cooper JA. How capping protein binds the barbed end of the actin filament. Current Biology 2003;13(17):1531-7.

9. Burtnick LD, Urosev D, Irobi E, Narayan K, Robinson RC. Structure of the N-terminal half of gelsolin bound to actin: Roles in severing, apoptosis and FAF. Embo j 2004 Jul 21;23(14):2713-22.

10. Zhang Y, Vorobiev SM, Gibson BG, Hao B, Sidhu GS, Mishra VS, Yarmola EG, Bubb MR, Almo SC, Southwick FS. A CapG gain-of-function mutant reveals critical structural and functional determinants for actin filament severing. Embo j 2006 Oct 4;25(19):4458-67.

11. Tanaka J, Yan Y, Choi J, Bai J, Klenchin VA, Rayment I, Marriott G. Biomolecular mimicry in the actin cytoskeleton: Mechanisms underlying the cytotoxicity of kabiramide C and related macrolides. Proc Natl Acad Sci U S A 2003 Nov 25;100(24):13851-6.

12. Petchprayoon C, Suwanborirux K, Miller R, Sakata T, Marriott G. Synthesis and characterization of the 7-(4-aminomethyl-1 H-1, 2, 3-triazol-1-yl) analogue of kabiramide C. J Nat Prod 2005;68(2):157-61.

13. Klenchin VA, Allingham JS, King R, Tanaka J, Marriott G, Rayment I. Trisoxazole macrolide toxins mimic the binding of actin-capping proteins to actin. Nature Structural & Molecular Biology 2003;10(12):1058-63.

14. Petchprayoon C, Suwanborirux K, Tanaka J, Yan Y, Sakata T, Marriott G. Fluorescent kabiramides: New probes to quantify actin in vitro and in vivo. Bioconjug Chem 2005;16(6):1382-9.

15. Tanaka J, Yan Y, Choi J, Bai J, Klenchin VA, Rayment I, Marriott G. Biomolecular mimicry in the actin cytoskeleton: Mechanisms underlying the cytotoxicity of kabiramide C and related macrolides. Proc Natl Acad Sci U S A 2003 Nov 25;100(24):13851-6.

16. Lukinavičius G, Reymond L, D'Este E, Masharina A, Göttfert F, Ta H, Güther A, Fournier M, Rizzo S, Waldmann H. Fluorogenic probes for live-cell imaging of the cytoskeleton. Nature Methods 2014;11(7):731-3.

17. Fath KR, Trimbur GM, Burgess DR. Molecular motors and a spectrin matrix associate with golgi membranes in vitro. J Cell Biol 1997 Dec 1;139(5):1169-81.

18. Merrifield CJ, Moss SE, Ballestrem C, Imhof BA, Giese G, Wunderlich I, Almers W. Endocytic vesicles move at the tips of actin tails in cultured mast cells. Nat Cell Biol 1999;1(1):72-4.

19. Welch MD, Iwamatsu A, Mitchison TJ. Actin polymerization is induced by arp 2/3 protein complex at the surface of listeria monocytogenes. Nature 1997;385(6613):265-9.

20. Gaullier J, Simonsen A, D'Arrigo A, Bremnes B, Stenmark H, Aasland R. FYVE fingers bind PtdIns (3) P. Nature 1998;394(6692):432-3.

21. Dumas JJ, Merithew E, Sudharshan E, Rajamani D, Hayes S, Lawe D, Corvera S, Lambright DG. Multivalent endosome targeting by homodimeric EEA1. Mol Cell 2001;8(5):947-58.

22. Cudmore S, Cossart P, Griffiths G, Way M. Actin-based motility of vaccinia virus. 1995.

23. Green RA, Paluch E, Oegema K. Cytokinesis in animal cells. Annu Rev Cell Dev Biol 2012;28:29-58.

24. Pelham RJ, Chang F. Actin dynamics in the contractile ring during cytokinesis in fission yeast. Nature 2002;419(6902):82-6.

25. Montagnac G, Echard A, Chavrier P. Endocytic traffic in animal cell cytokinesis. Curr Opin Cell Biol 2008;20(4):454-61.

26. Boucrot E, Kirchhausen T. Endosomal recycling controls plasma membrane area during mitosis. Proc Natl Acad Sci U S A 2007 May 8;104(19):7939-44.

27. Ingber DE. Cellular mechanotransduction: Putting all the pieces together again. Faseb j 2006 May;20(7):811-27.

28. Ingber DE. Tensegrity: The architectural basis of cellular mechanotransduction. Annu Rev Physiol 1997;59(1):575-99.

29. DuFort CC, Paszek MJ, Weaver VM. Balancing forces: Architectural control of mechanotransduction. Nature Reviews Molecular Cell Biology 2011;12(5):308-19.

30. Janmey PA, McCulloch CA. Cell mechanics: Integrating cell responses to mechanical stimuli. Annu Rev Biomed Eng 2007;9:1-34.

31. Geiger B, Bershadsky A. Exploring the neighborhood: Adhesion-coupled cell mechanosensors. Cell 2002;110(2):139-42.

32. Smith ML, Gourdon D, Little WC, Kubow KE, Eguiluz RA, Luna-Morris S, Vogel V. Force-induced unfolding of fibronectin in the extracellular matrix of living cells. PLoS Biol 2007;5(10):e268.

33. Chiquet M. Regulation of extracellular matrix gene expression by mechanical stress. Matrix Biology 1999;18(5):417-26.

34. Wang JH, Thampatty BP, Lin J, Im H. Mechanoregulation of gene expression in fibroblasts. Gene 2007;391(1):1-15.

35. Chiquet M, Renedo AS, Huber F, Flück M. How do fibroblasts translate mechanical signals into changes in extracellular matrix production? Matrix Biology 2003;22(1):73-80.

36. Gerace L, Burke B. Functional organization of the nuclear envelope. Annu Rev Cell Biol 1988;4(1):335-74.

37. Crisp M, Liu Q, Roux K, Rattner JB, Shanahan C, Burke B, Stahl PD, Hodzic D. Coupling of the nucleus and cytoplasm: Role of the LINC complex. J Cell Biol 2006 Jan 2;172(1):41-53.

38. Mellad JA, Warren DT, Shanahan CM. Nesprins LINC the nucleus and cytoskeleton. Curr Opin Cell Biol 2011;23(1):47-54.

39. Méjat A. LINC complexes in health and disease. Nucleus 2010;1(1):40-52.

40. Brosig M, Ferralli J, Gelman L, Chiquet M, Chiquet-Ehrismann R. Interfering with the connection between the nucleus and the cytoskeleton affects nuclear rotation, mechanotransduction and myogenesis. Int J Biochem Cell Biol 2010;42(10):1717-28.

41. Reinsch S, Gonczy P. Mechanisms of nuclear positioning. J Cell Sci 1998 Aug;111 (Pt 16)(Pt 16):2283-95.

42. Luxton GW, Gomes ER, Folker ES, Vintinner E, Gundersen GG. Linear arrays of nuclear envelope proteins harness retrograde actin flow for nuclear movement. Science 2010 Aug 20;329(5994):956-9.

43. Nikolova-Krstevski V, Leimena C, Xiao X, Kesteven S, Tan JC, Yeo LS, Yu Z, Zhang Q, Carlton A, Head S. Nesprin-1 and actin contribute to nuclear and cytoskeletal defects in lamin A/C-deficient cardiomyopathy. J Mol Cell Cardiol 2011;50(3):479-86.

44. Zaman MH, Trapani LM, Sieminski AL, Mackellar D, Gong H, Kamm RD, Wells A, Lauffenburger DA, Matsudaira P. Migration of tumor cells in 3D matrices is governed by matrix stiffness along with cell-matrix adhesion and proteolysis. Proc Natl Acad Sci U S A 2006 Jul 18;103(29):10889-94.

45. Kass L, Erler JT, Dembo M, Weaver VM. Mammary epithelial cell: Influence of extracellular matrix composition and organization during development and tumorigenesis. Int J Biochem Cell Biol 2007;39(11):1987-94.

46. Ulrich TA, de Juan Pardo EM, Kumar S. The mechanical rigidity of the extracellular matrix regulates the structure, motility, and proliferation of glioma cells. Cancer Res 2009 May 15;69(10):4167-74.

47. Tay CY, Yu H, Pal M, Leong WS, Tan NS, Ng KW, Leong DT, Tan LP. Micropatterned matrix directs differentiation of human mesenchymal stem cells towards myocardial lineage. Exp Cell Res 2010;316(7):1159-68.

48. Downing TL, Soto J, Morez C, Houssin T, Fritz A, Yuan F, Chu J, Patel S, Schaffer DV, Li S. Biophysical regulation of epigenetic state and cell reprogramming. Nature Materials 2013;12(12):1154-62.

49. Jaalouk DE, Lammerding J. Mechanotransduction gone awry. Nature Reviews Molecular Cell Biology 2009;10(1):63-73.

50. Méjat A. LINC complexes in health and disease. Nucleus 2010;1(1):40-52.

51. Wulf E, Deboben A, Bautz FA, Faulstich H, Wieland T. Fluorescent phallotoxin, a tool for the visualization of cellular actin. Proc Natl Acad Sci U S A 1979 Sep;76(9):4498-502.

52. Choidas A, Jungbluth A, Sechi A, Murphy J, Ullrich A, Marriott G. The suitability and application of a GFP-actin fusion protein for long-term imaging of the organization and dynamics of the cytoskeleton in mammalian cells. Eur J Cell Biol 1998;77(2):81-90.

53. Riedl J, Crevenna AH, Kessenbrock K, Yu JH, Neukirchen D, Bista M, Bradke F, Jenne D, Holak TA, Werb Z. Lifeact: A versatile marker to visualize F-actin. Nature Methods 2008;5(7):605-7.

54. Lukinavičius G, Reymond L, D'Este E, Masharina A, Göttfert F, Ta H, Güther A, Fournier M, Rizzo S, Waldmann H. Fluorogenic probes for live-cell imaging of the cytoskeleton. Nature Methods 2014;11(7):731-3.

55. Fricker M, Hollinshead M, White N, Vaux D. Interphase nuclei of many mammalian cell types contain deep, dynamic, tubular membrane-bound invaginations of the nuclear envelope. J Cell Biol 1997 Feb 10;136(3):531-44.

56. Kovacs M, Toth J, Hetenyi C, Malnasi-Csizmadia A, Sellers JR. Mechanism of blebbistatin inhibition of myosin II. J Biol Chem 2004 Aug 20;279(34):35557-63.

57. Zhang M, Rao PV. Blebbistatin, a novel inhibitor of myosin II ATPase activity, increases aqueous humor outflow facility in perfused enucleated porcine eyes. Invest Ophthalmol Vis Sci 2005;46(11):4130-8.

58. Dahl KN, Kahn SM, Wilson KL, Discher DE. The nuclear envelope lamina network has elasticity and a compressibility limit suggestive of a molecular shock absorber. J Cell Sci 2004 Sep 15;117(Pt 20):4779-86.

59. Schliwa M. Action of cytochalasin D on cytoskeletal networks. J Cell Biol 1982 Jan;92(1):79-91.

60. Casella JF, Flanagan MD, Lin S. Cytochalasin D inhibits actin polymerization and induces depolymerization of actin filaments formed during platelet shape change. 1981.

61. Sampath P, Pollard TD. Effects of cytochalasin, phalloidin and pH on the elongation of actin filaments. Biochemistry (N Y) 1991;30(7):1973-80.

62. Riento K, Ridley AJ. Rocks: Multifunctional kinases in cell behaviour. Nature Reviews Molecular Cell Biology 2003;4(6):446-56.

63. Maekawa M, Ishizaki T, Boku S, Watanabe N, Fujita A, Iwamatsu A, Obinata T, Ohashi K, Mizuno K, Narumiya S. Signaling from rho to the actin cytoskeleton through protein kinases ROCK and LIM-kinase. Science 1999 Aug 6;285(5429):895-8.

64. Wang Y, Zheng XR, Riddick N, Bryden M, Baur W, Zhang X, Surks HK. ROCK isoform regulation of myosin phosphatase and contractility in vascular smooth muscle cells. Circ Res 2009 Feb 27;104(4):531-40.

65. Ishizaki T, Uehata M, Tamechika I, Keel J, Nonomura K, Maekawa M, Narumiya S. Pharmacological properties of Y-27632, a specific inhibitor of rho-associated kinases. Mol Pharmacol 2000 May;57(5):976-83.

66. Crews P, Manes LV, Boehler M. Jasplakinolide, a cyclodepsipeptide from the marine sponge, jaspis sp. Tetrahedron Lett 1986;27(25):2797-800.

67. Bubb MR, Spector I, Beyer BB, Fosen KM. Effects of jasplakinolide on the kinetics of actin polymerization. an explanation for certain in vivo observations. J Biol Chem 2000 Feb 18;275(7):5163-70.

68. Bubb MR, Senderowicz AM, Sausville EA, Duncan KL, Korn ED. Jasplakinolide, a cytotoxic natural product, induces actin polymerization and competitively inhibits the binding of phalloidin to F-actin. J Biol Chem 1994 May 27;269(21):14869-71.

69. Rando OJ, Zhao K, Crabtree GR. Searching for a function for nuclear actin. Trends Cell Biol 2000;10(3):92-7.

70. Olave IA, Reck-Peterson SL, Crabtree GR. Nuclear actin and actin-related proteins in chromatin remodeling. Annu Rev Biochem 2002;71(1):755-81.

71. Percipalle P, Visa N. Molecular functions of nuclear actin in transcription. J Cell Biol 2006 Mar 27;172(7):967-71.

72. Gieni RS, Hendzel MJ. Actin dynamics and functions in the interphase nucleus: Moving toward an understanding of nuclear polymeric actin this paper is one of a selection of papers published in this special issue, entitled 29th annual international asilomar chromatin and chromosomes conference, and has undergone the journal's usual peer review process. Biochemistry and Cell Biology 2009;87(1):283-306.

73. Clark TG, Rosenbaum JL. An actin filament matrix in hand-isolated nuclei of X. laevis oocytes. Cell 1979;18(4):1101-8.

74. Clark TG, Merriam RW. Diffusible and bound actin in nuclei of xenopus laevis oocytes. Cell 1977;12(4):883-91.

75. Goode BL, Eck MJ. Mechanism and function of formins in the control of actin assembly. Annu Rev Biochem 2007;76:593-627.

76. Johnson N, Krebs M, Boudreau R, Giorgi G, LeGros M, Larabell C. Actin-filled nuclear invaginations indicate degree of cell de-differentiation. Differentiation 2003;71(7):414-24.

77. Pinto IM, Rubinstein B, Kucharavy A, Unruh JR, Li R. Actin depolymerization drives actomyosin ring contraction during budding yeast cytokinesis. Developmental Cell 2012;22(6):1247-60.

78. Yager P, Domingo GJ, Gerdes J. Point-of-care diagnostics for global health. Annu Rev Biomed Eng 2008;10:107-44.

79. Wang J. Electrochemical biosensors: Towards point-of-care cancer diagnostics. Biosensors and Bioelectronics 2006;21(10):1887-92.

80. Thrush E, Levi O, Cook LJ, Deich J, Kurtz A, Smith SJ, Moerner W, Harris JS. Monolithically integrated semiconductor fluorescence sensor for microfluidic applications. Sensors Actuators B: Chem 2005;105(2):393-9.

81. Coskun AF, Cetin AE, Galarreta BC, Alvarez DA, Altug H, Ozcan A. Lensfree optofluidic plasmonic sensor for real-time and label-free monitoring of molecular binding events over a wide field-of-view. Scientific Reports 2014;4.

82. Cui Y, Wei Q, Park H, Lieber CM. Nanowire nanosensors for highly sensitive and selective detection of biological and chemical species. Science 2001 Aug 17;293(5533):1289-92.

83. Yan Y, Marriott G. Analysis of protein interactions using fluorescence technologies. Curr Opin Chem Biol 2003;7(5):635-40.

84. Wilson WD. Analyzing biomolecular interactions. Science 2002;295(5562):2103.

85. Fan B, Liu F, Li Y, Wang X, Cui K, Feng X, Zhang W, Huang Y. Integrated refractive index sensor based on hybrid coupler with short range surface plasmon polariton and dielectric waveguide. Sensors Actuators B: Chem 2013;186:495-505.

86. Cunningham B, Lin B, Qiu J, Li P, Pepper J, Hugh B. A plastic colorimetric resonant optical biosensor for multiparallel detection of label-free biochemical interactions. Sensors Actuators B: Chem 2002;85(3):219-26.

87. Cunningham BT, Li P, Schulz S, Lin B, Baird C, Gerstenmaier J, Genick C, Wang F, Fine E, Laing L. Label-free assays on the BIND system. J Biomol Screen 2004 Sep;9(6):481-90.

88. White IM, Oveys H, Fan X, Smith TL, Zhang J. Integrated multiplexed biosensors based on liquid core optical ring resonators and antiresonant reflecting optical waveguides. Appl Phys Lett 2006;89(19):191106.

89. Vollmer F, Arnold S. Whispering-gallery-mode biosensing: Label-free detection down to single molecules. Nature Methods 2008;5(7):591-6.

90. Chang T, Huang M, Yanik AA, Tsai H, Shi P, Aksu S, Yanik MF, Altug H. Large-scale plasmonic microarrays for label-free high-throughput screening. Lab on a Chip 2011;11(21):3596-602.

91. Von Lode P. Point-of-care immunotesting: Approaching the analytical performance of central laboratory methods. Clin Biochem 2005;38(7):591-606.

92. Chang-Hasnain CJ, Yang W. High-contrast gratings for integrated optoelectronics. Advances in Optics and Photonics 2012;4(3):379-440.

93. Melanson SE, Tanasijevic MJ, Jarolim P. Cardiac troponin assays: A view from the clinical chemistry laboratory. Circulation 2007 Oct 30;116(18):e501-4.

94. Go AS, Mozaffarian D, Roger VL, Benjamin EJ, Berry JD, Borden WB, Bravata DM, Dai S, Ford ES, Fox CS, et al. Heart disease and stroke statistics--2013 update: A report from the american heart association. Circulation 2013 Jan 1;127(1):e6-e245.

95. Wang K, Li H, Yuan Y, Etheridge A, Zhou Y, Huang D, Wilmes P, Galas D. The complex exogenous RNA spectra in human plasma: An interface with human gut biota? 2012.

96. Reichlin T, Hochholzer W, Bassetti S, Steuer S, Stelzig C, Hartwiger S, Biedert S, Schaub N, Buerge C, Potocki M. Early diagnosis of myocardial infarction with sensitive cardiac troponin assays. N Engl J Med 2009;361(9):858-67.

97. Scharnhorst V, Krasznai K, van't Veer M, Michels R. Rapid detection of myocardial infarction with a sensitive troponin test. Am J Clin Pathol 2011 Mar;135(3):424-8.

98. Straface AL, Myers JH, Kirchick HJ, Blick KE. A rapid point-of-care cardiac marker testing strategy facilitates the rapid diagnosis and management of chest pain patients in the emergency department. Am J Clin Pathol 2008 May;129(5):788-95.

99. Böhm I, Schild H. Apoptosis: The complex scenario for a silent cell death. Molecular Imaging & Biology 2003;5(1):2-14.

100. Kroemer G, Galluzzi L, Vandenabeele P, Abrams J, Alnemri ES, Baehrecke EH, Blagosklonny MV, El-Deiry WS, Golstein P, Green DR, et al. Classification of cell death: Recommendations of the nomenclature committee on cell death 2009. Cell Death Differ 2009 Jan;16(1):3-11.

101. Krysko DV, Vanden Berghe T, D'Herde K, Vandenabeele P. Apoptosis and necrosis: Detection, discrimination and phagocytosis. Methods 2008 Mar;44(3):205-21.

102. Thompson CB. Apoptosis in the pathogenesis and treatment of disease. Science 1995 Mar 10;267(5203):1456-62.

103. Galluzzi L, Vanden Berghe T, Vanlangenakker N, Buettner S, Eisenberg T, Vandenabeele P, Madeo F, Kroemer G. Programmed necrosis from molecules to health and disease. Int Rev Cell Mol Biol 2011;289:1-35.

104. Upton JW, Kaiser WJ, Mocarski ES. Virus inhibition of RIP3-dependent necrosis. Cell Host Microbe 2010 Apr 22;7(4):302-13.

105. Upton JW, Kaiser WJ, Mocarski ES. DAI/ZBP1/DLM-1 complexes with RIP3 to mediate virus-induced programmed necrosis that is targeted by murine cytomegalovirus vIRA. Cell Host Microbe 2012 Mar 15;11(3):290-7.

106. Gorbunova V, Hine C, Tian X, Ablaeva J, Gudkov AV, Nevo E, Seluanov A. Cancer resistance in the blind mole rat is mediated by concerted necrotic cell death mechanism. Proc Natl Acad Sci U S A 2012 Nov 20;109(47):19392-6.

107. Proskuryakov SY, Konoplyannikov AG, Gabai VL. Necrosis: A specific form of programmed cell death? Exp Cell Res 2003;283(1):1-16.

108. Christofferson DE, Yuan J. Necroptosis as an alternative form of programmed cell death. Curr Opin Cell Biol 2010;22(2):263-8.

109. Chan FK, Shisler J, Bixby JG, Felices M, Zheng L, Appel M, Orenstein J, Moss B, Lenardo MJ. A role for tumor necrosis factor receptor-2 and receptor-interacting protein in programmed necrosis and antiviral responses. J Biol Chem 2003 Dec 19;278(51):51613-21.

110. Kawahara A, Ohsawa Y, Matsumura H, Uchiyama Y, Nagata S. Caspase-independent cell killing by fas-associated protein with death domain. J Cell Biol 1998 Nov 30;143(5):1353-60.

111. Ch'en IL, Beisner DR, Degterev A, Lynch C, Yuan J, Hoffmann A, Hedrick SM. Antigen-mediated T cell expansion regulated by parallel pathways of death. Proc Natl Acad Sci U S A 2008 Nov 11;105(45):17463-8.

112. Micheau O, Tschopp J. Induction of TNF receptor I-mediated apoptosis via two sequential signaling complexes. Cell 2003;114(2):181-90.

113. Cho Y, Challa S, Moquin D, Genga R, Ray TD, Guildford M, Chan FK. Phosphorylation-driven assembly of the RIP1-RIP3 complex regulates programmed necrosis and virus-induced inflammation. Cell 2009;137(6):1112-23.

114. Feng S, Yang Y, Mei Y, Ma L, Zhu D, Hoti N, Castanares M, Wu M. Cleavage of RIP3 inactivates its caspase-independent apoptosis pathway by removal of kinase domain. Cell Signal 2007;19(10):2056-67.

115. Sun X, Yin J, Starovasnik MA, Fairbrother WJ, Dixit VM. Identification of a novel homotypic interaction motif required for the phosphorylation of receptor-interacting protein (RIP) by RIP3. J Biol Chem 2002 Mar 15;277(11):9505-11.

116. Holler N, Zaru R, Micheau O, Thome M, Attinger A, Valitutti S, Bodmer J, Schneider P, Seed B, Tschopp J. Fas triggers an alternative, caspase-8–independent cell death pathway using the kinase RIP as effector molecule. Nat Immunol 2000;1(6):489-95.

117. Vandenabeele P, Galluzzi L, Berghe TV, Kroemer G. Molecular mechanisms of necroptosis: An ordered cellular explosion. Nature Reviews Molecular Cell Biology 2010;11(10):700-14.

118. Kroemer G, Galluzzi L, Brenner C. Mitochondrial membrane permeabilization in cell death. Physiol Rev 2007 Jan;87(1):99-163.

119. Degterev A, Huang Z, Boyce M, Li Y, Jagtap P, Mizushima N, Cuny GD, Mitchison TJ, Moskowitz MA, Yuan J. Chemical inhibitor of nonapoptotic cell death with therapeutic potential for ischemic brain injury. Nature Chemical Biology 2005;1(2):112-9.

120. Budihardjo I, Oliver H, Lutter M, Luo X, Wang X. Biochemical pathways of caspase activation during apoptosis. Annu Rev Cell Dev Biol 1999;15(1):269-90.

121. Levine B, Klionsky DJ. Development by self-digestion: Molecular mechanisms and biological functions of autophagy. Developmental Cell 2004;6(4):463-77.

122. TNF T, Jurkat, CHX FADD-def Jurkat WT. Cyclophilin A release as a biomarker of necrotic cell death. Cell Death Differ 2010;17:1942-3.

123. Zhang DW, Shao J, Lin J, Zhang N, Lu BJ, Lin SC, Dong MQ, Han J. RIP3, an energy metabolism regulator that switches TNF-induced cell death from apoptosis to necrosis. Science 2009 Jul 17;325(5938):332-6.

124. Zhang D, Lin J, Han J. Receptor-interacting protein (RIP) kinase family. Cellular & Molecular Immunology 2010;7(4):243-9.

125. Holland PM, Willis CR, Kanaly S, Glaccum MB, Warren AS, Charrier K, Murison JG, Derry JM, Virca GD, Bird TA. RIP4 is an ankyrin repeat-containing kinase essential for keratinocyte differentiation. Current Biology 2002;12(16):1424-8.

126. Chen L, Haider K, Ponda M, Cariappa A, Rowitch D, Pillai S. Protein kinase C-associated kinase (PKK), a novel membrane-associated, ankyrin repeat-containing protein kinase. J Biol Chem 2001 Jun 15;276(24):21737-44.

127. Chen L, Haider K, Ponda M, Cariappa A, Rowitch D, Pillai S. Protein kinase C-associated kinase (PKK), a novel membrane-associated, ankyrin repeat-containing protein kinase. J Biol Chem 2001 Jun 15;276(24):21737-44.

128. Bhr C, Rohwer A, Stempka L, Rincke G, Marks F, Gschwendt M. DIK, a novel protein kinase that interacts with protein kinase cdelta. cloning, characterization, and gene analysis. J Biol Chem 2000 Nov 17;275(46):36350-7.

129. Adams S, Munz B. RIP4 is a target of multiple signal transduction pathways in keratinocytes: Implications for epidermal differentiation and cutaneous wound repair. Exp Cell Res 2010;316(1):126-37.

130. Ehlers S, Mueck T, Adams S, Landuzzi L, Lollini P, Munz B. RIP2 regulates growth and differentiation of normal myoblasts and of rhabdomyosarcoma cells. Eur J Cell Biol 2008;87(3):163-72.

131. Zha J, Zhou Q, Xu L, Chen D, Li L, Zhai Z, Shu H. RIP5 is a RIP-homologous inducer of cell death. Biochem Biophys Res Commun 2004;319(2):298-303.

132. Meylan E, Tschopp J. The RIP kinases: Crucial integrators of cellular stress. Trends Biochem Sci 2005;30(3):151-9.

133. Greggio E, Zambrano I, Kaganovich A, Beilina A, Taymans JM, Daniels V, Lewis P, Jain S, Ding J, Syed A, et al. The parkinson disease-associated leucine-rich repeat kinase 2 (LRRK2) is a dimer that undergoes intramolecular autophosphorylation. J Biol Chem 2008 Jun 13;283(24):16906-14.

134. Kamikawaji S, Ito G, Iwatsubo T. Identification of the autophosphorylation sites of LRRK2. Biochemistry (N Y) 2009;48(46):10963-75.

135. Cookson MR. The role of leucine-rich repeat kinase 2 (LRRK2) in parkinson's disease. Nature Reviews Neuroscience 2010;11(12):791-7.

136. Wang Z, Jiang H, Chen S, Du F, Wang X. The mitochondrial phosphatase PGAM5 functions at the convergence point of multiple necrotic death pathways. Cell

2012;148(1):228-43.

137. Zhang J, Kan S, Huang B, Hao Z, Mak TW, Zhong Q. Mule determines the apoptotic response to HDAC inhibitors by targeted ubiquitination and destruction of HDAC2. Genes Dev 2011 Dec 15;25(24):2610-8.

138. Zhong Q, Gao W, Du F, Wang X. Mule/ARF-BP1, a BH3-only E3 ubiquitin ligase, catalyzes the polyubiquitination of mcl-1 and regulates apoptosis. Cell 2005;121(7):1085-95.

139. Galluzzi L, Kepp O, Trojel-Hansen C, Kroemer G. Mitochondrial control of cellular life, stress, and death. Circ Res 2012 Oct 12;111(9):1198-207.